Materials Advances

ROYAL SOCIETY OF CHEMISTRY

PAPER

View Article Online
View Journal | View Issue

Cite this: *Mater. Adv.*, 2025, **6**, 1520

Achieving 27.20% efficiency for a lead-free double perovskite solar cell with all inorganic Cs_2BiAgI_6 using AZO UTL as a passivation layer†

Aminreza Mohandes and Mahmood Moradi*

A major challenge in the commercialization of perovskite solar cells (PSCs) is the presence of toxic metals, like lead, in their composition. Compared with conventional lead halide perovskites, double halide perovskites have garnered significant interest owing to their reduced toxicity, adjustable bandgap, structural flexibility, and enhanced stability. This study focuses on evaluating a lead-free Cs_2BiAgI_6-double perovskite solar cell (DPSC) using a one-dimensional solar cell capacitance simulator (SCAPS-1D) with a bilayer ZnO/AZO electron transport layer (ETL) and ZnO ETL, along with various hole transport layers (HTLs) for the first time. The selected HTLs included CBTS, Cu_2O, $CuAlO_2$, CZTS, CuSCN, spiro-OMeTAD, MoO_3, and V_2O_5. Various factors, such as energy band alignment, recombination and generation rates, absorber thickness, defect and doping densities for all layers, energy levels of ETLs and HTL, interfacial defect densities, back metal contact, and operating temperature, were examined for improving the performance of DPSC. This study was aimed at enhancing the efficiency and deepening our understanding of the electron transport mechanisms in Cs_2BiAgI_6-DPSCs. The research findings suggested that V_2O_5 and ZnO/AZO were the most suitable materials for the HTL and ETL, respectively, among the various options considered. Therefore, we utilized ITO/ZnO/AZO/Cs_2BiAgI_6/V_2O_5/Au as the required DPSC. To boost the performance of the DPSC, electron–hole pair handling at the ETL/perovskite interface was optimized by adding a 10 nm AZO UTL, thereby enhancing the ZnO/double perovskite interface properties. The bilayer structure of ZnO/AZO offered advantages such as efficient electron extraction and minimal interfacial recombination owing to its enhanced energy level alignment and defect passivation. After optimizing these parameters, the system with the ZnO/AZO bilayer ETL achieved an efficiency of 27.20%, along with a V_{oc} of 1.3221 V, J_{sc} of 23.84 mA cm^{-2}, and FF of 86.28%. Thus, this work presents a straightforward and promising approach for fabricating photovoltaic devices, particularly for various types of double perovskites, with favorable charge transport layers and recombination properties. Furthermore, these findings offer theoretical guidance to improve the efficiency of Cs_2BiAgI_6-based photovoltaic solar cells (DPSCs) and facilitate the widespread adoption of eco-friendly and stable perovskites.

Received 26th December 2024,
Accepted 20th January 2025

DOI: 10.1039/d4ma01280a

rsc.li/materials-advances

1. Introduction

To meet the energy demands of daily life, we use fossil fuels, such as natural gas and coal, which are harmful to society and the environment.[1,2] Hence, the focus of global research is shifted to the development of alternative energy sources and sustainable energy options that address both economic and environmental concerns. Solar cells are a key renewable energy source, especially perovskite ones, which have attained a significant increase in efficiency from 3.8% to 26.1% since 2009.[1,2] The ABX_3 formula of perovskite solar cells (PSCs) has a monovalent cation ($MA^+ = CH_3NH_3^+$, $FA^+ = H_2NCHNH_2^+$, and Cs^+) as A, a divalent metal cation (lead (Pb^{2+}), tin (Sn^{2+}), titanium (Ti^{2+}), bismuth (Bi^{2+}), and silver (Ag^{2+})) as B, and a halogen anion (Cl^-, Br^-, and I^-) as X. Lead–halide and organic–inorganic hybrid PSCs have gained attention owing to their high power conversion efficiency (PCE) of 26.1%, which is comparable to top silicon solar cells.[3–5] Despite this remarkable efficiency of PSCs, the presence of toxic lead materials and volatile organic cations in their composition hinders their widespread application.[6–11] Organic–inorganic PSCs are unstable owing to the presence of oxygen, moisture, and heat generated by organic cations.[12] Moreover, lead-based perovskites are very toxic and pose health risks.[13–15]

Department of Physics, College of Science, Shiraz University, 71946-84795 Shiraz, Iran. E-mail: mmoradi@shirazu.ac.ir

† Electronic supplementary information (ESI) available. See DOI: https://doi.org/10.1039/d4ma01280a

The demand for non-toxic PSCs has led to the research on lead-free materials. To replace lead-based perovskites, Sn^{2+} and Ge^{2+} (germanium) were used instead of Pb^{2+} in previous studies. However, Sn^{2+} and Ge^{2+} in lead-free PSCs had limited stability owing to oxidation.[16] Pb^{2+} were also replaced with non-toxic Bi^{3+} ions, which are isoelectronic and stable.[17] Bismuth PSCs showed longer charge carrier diffusion owing to their reduced trap densities.[18] Introducing Bi^{3+} in $A^{1+}B^{2+}X_3$ resulted in optoelectronic properties that were worse than those of lead perovskites.[19,20] To recover from these inferior characteristics, Bi^{3+} anion was added to an elpasolite structure or a double perovskite structure.[21] Elpasolite structure has the formula $A_2B^{1+}B^{3+}X_6$, where A represents a monovalent cation, X represents a halide anion, B^{1+} represents an inorganic cation, and B^{3+} represents an organic or inorganic cation. According to recent investigations, double perovskites incorporating Bi^{3+} and Ag^{1+} ions exhibit considerable promise for application in photovoltaic technologies because of their advantageous bandgaps, comparable charge carrier effective masses, exceptional photoluminescence lifetimes, extended carrier recombination lifetimes, and robust stabilities.[22–27] McClure *et al.* have stated that $Cs_2AgBiBr_6$ and $Cs_2AgBiCl_6$ show a noticeable bandgap and exhibit higher stability than $MAPbX_3$.[21] However, $Cs_2AgBiBr_6$ and $Cs_2AgBiCl_6$ exhibit low efficacy owing to their high charge carrier effective masses, restricted charge carrier transport capabilities, and substantial band gap,[28–30] making them unsuitable for integration into solar cells. The absorber Cs_2AgBiI_6 exhibits a band gap of 1.12 eV, excellent light absorption capability and enhanced efficacy compared to $Cs_2AgBiBr_6$ and $Cs_2AgBiCl_6$, indicating its potential for double perovskite solar cell (DPSC).[31,32]

The physical properties of a material in a device are key to understanding its state and potential practical applications. Researchers have used density functional theory (DFT) to study material properties, such as halide perovskites. These materials have special properties spotless for optoelectronic and photovoltaic applications.[33–35] Hadi *et al.*[36] studied $Cs_2AgBiBr_6$ using DFT to explore its properties by inducing disorder in the compound through the creation of an antisite defect in the sublattice; the indirect band gap of $Cs_2AgBiBr_6$ was reduced and converted to a direct band gap. This modification enhanced the optical absorption in the visible region, making $Cs_2AgBiBr_6$ suitable for solar cell applications.

Here, we conduct a literature review focusing on the ZnO/AZO bilayer structure, exploring its various properties, applications, potential advancements, and efficiency enhancement in the field of PSCs.[37]

Dong *et al.*[38] reported that ZnO (zinc oxide) nanorods modified with aluminum-doped ZnO (AZO) are utilized in PSCs containing $MAPbI_3$. This modification has demonstrated a beneficial impact on both the V_{oc} (open-circuit voltage) and the PCE. The average PCE is enhanced from 8.5% to 10.07%, with the maximum efficiency reaching 10.7%. Tseng *et al.*[39] reported that Al doping proved to be effective in altering the physicochemical characteristics of ZnO to enhance its performance. A high-quality, fully coated thin film of AZO on an ITO (indium tin oxide) substrate was successfully fabricated using a sputtering technique. When compared to a cell utilizing ZnO, a perovskite cell incorporating AZO as the ETL exhibits superior stability. The most efficient PSC based on AZO achieves a PCE of 17.6% for the ZnO ETL-based PSC. Wu *et al.*[40] reported that the ZnO/perovskite interface has several drawbacks, including the decomposition of $MAPbI_3$ and misaligned energy levels. To solve these issues, we suggest a new design using a low-temperature ZnO/AZO bilayer thin film with band alignment as electron transport layers in PSCs. This enhances PSC efficiency. The PCE increases from 12.3% to 16.1% with the incorporation of the AZO thin film. In addition, some researchers have worked experimentally on the performance of PSCs to improve efficiency using ZnO/AZO bilayer.[41–44]

To the best of our knowledge, for the first time, the evaluation of lead-free Cs_2BiAgI_6-DPSC using a one-dimensional solar cell capacitance simulator (SCAPS-1D) with bilayer ZnO/AZO ETL and ZnO ETL with various HTLs is carried out and compared. Various HTLs, including CBTS (copper barium thiostannate), Cu_2O (copper(I) oxide), $CuAlO_2$ (copper aluminum oxide), CZTS (copper zinc tin sulfide), CuSCN (copper(I) thiocyanate), Spiro-OMeTAD (2,2′,7,7′-tetrakis[*N*,*N*-di(4-ethoxyphenyl)amino]-9,9′-spirobifluorene), MoO_3 (molybdenum trioxide), and V_2O_5 (vanadium oxide) are selected. Next, we investigated the impact of various factors to enhance the performance of the DPSC. These factors included the energy band alignment, total recombination and total generation rate, thickness of the absorber, defect and doping densities of all layers, the energy levels of both ETLs and HTL, the interfacial defect densities of both the ETL and HTL sides, the back metal contact, and operating temperature. This study has the potential to enhance efficiency and deepen our understanding of the electron transport mechanism in Cs_2BiAgI_6-DPSCs. Additionally, simulation work was carried out on the most efficient cells to gain a more comprehensive understanding of the device's electrical properties. Ultimately, it was revealed that these interfacial bilayers significantly enhanced the photovoltaic characteristics and overall performance of the DPSC.

2. Materials and methodology

2.1. Methodology

Various simulation software, such as SCAPS-1D, PC-1D, AMPS-1D, wxAMPS, COMSOL, and Silvaco, are utilized to simulate the device structures and evaluate the photovoltaic performance of different kinds of solar cells.[45] In this particular study, SCAPS-1D version-3.3.08, developed by the Department of Electronics and Information Systems (ELIS) at the University of Gent, Belgium, is employed to simulate and model the DPSC with Cs_2BiAgI_6 as the active layer.[46] The simulation process involves using three semiconductor equations: eqn (1) represents the Poisson equation, which establishes the relationship between carrier concentrations and electrostatic potential, while eqn (2) and (3) correspond to the continuity equations for electrons and holes, respectively. These equations enable the analysis of the charge carrier generation and recombination mechanisms

in the semiconductor.

$$\frac{\partial}{\partial x}\left(-\varepsilon(x)\cdot\frac{\partial\psi}{\partial x}\right) = q[p(x)-n(x)+N_D{}^{+}(x) - N_A{}^{-}(x)+p_t(x)-n_t(x)], \quad (1)$$

$$\frac{\partial n_p}{\partial t} = G_n - \frac{n_p - n_{p0}}{\tau_n} + n_p\mu_n\frac{\partial\xi}{\partial x} + \mu_n\xi\frac{\partial n_p}{\partial x} + D_n\frac{\partial^2 n_p}{\partial x^2}, \quad (2)$$

$$\frac{\partial p_n}{\partial t} = G_p - \frac{p_n - p_{n0}}{\tau_p} + p_n\mu_p\frac{\partial\xi}{\partial x} + \mu_p\xi\frac{\partial p_n}{\partial x} + D_p\frac{\partial^2 p_n}{\partial x^2}, \quad (3)$$

where ψ denotes electric potential; ξ denotes the electric field; ε denotes the permittivity; q denotes the electronic charge; $p(x)$ and $n(x)$ are concentrations of charge carriers; $\tau_{n,p}$ represents the carrier lifetime, $\mu_{n,p}$ denotes charge mobilities; $N_A{}^{-}$ and $N_D{}^{+}$ denote shallow acceptor and shallow donor concentrations, respectively; $D_{n,p}$ denotes the diffusion coefficient of the charge carrier; G_n or G_p denotes the charge carrier generation rate, and $p_t(x)$ denote the defect densities of electrons and holes, respectively. At the (x) and $p_t(x)$ equilibrium state, we have the following equation:

$$\frac{\partial n_p}{\partial t} = \frac{\partial p_n}{\partial t} = 0. \quad (4)$$

2.2. Device structure and material parameters

In the formation of a double perovskite solar cell, the Cs_2BiAgI_6 absorber layer is accompanied by ETL, HTL, and back contact to create the DPSC structure, as it captures photons effectively owing to its double heterostructure, ensuring charge and photon confinement. The performance of various double perovskite solar cell structures (DPSCs) is investigated using SCAPS-1D software, with the ambient temperature set at 300 K and the AM 1.5G sunlight spectrum. Different structures are studied by incorporating two ETLs and eight HTLs, with a gold back contact.

The Cs_2BiAgI_6-DPSC is composed of multiple layers, including indium tin oxide (ITO), ZnO as ETL, Cs_2BiAgI_6 as the double perovskite absorbing (DPPVK) layer, and CBTS as HTL.[47] Notably, the DPPVK layer, Cs_2BiAgI_6, exhibits p-type carrier characteristics, with a bulk defect density of 1×10^{15} cm^{-3}. This parameter significantly affects the charge carrier lifetime of electrons and holes, resulting in a value of 100 ns for both. The diffusion lengths of the electron and hole charge carriers, denoted by L_n and L_p, respectively, are measured to be 0.72 μm. For simulation purposes, the DPPVK layer is assumed to have a thickness of 800 nm, as shown in Table 1. The thermal velocity of electrons and holes is confirmed to be 1×10^7 cm s^{-1}. Additionally, the defect energy level is positioned at the center of E_g, following a Gaussian distribution with a characteristic

Table 1 Material parameters used in the simulation

Material parameters	ITO	ZnO	Cs_2BiAgI_6	CBTS
Thickness (nm)	500	50	800	100
Energy band gap, E_g (eV)	3.5	3.3	1.6	1.9
Electronaffinity, χ (eV)	4	4	3.9	3.6
Relativedielectricpermittivity, ε_r	9	9	6.5	5.4
Conduction band effective density of state, N_C (cm^{-3})	2.2×10^{18}	3.7×10^{18}	1×10^{19}	2.2×10^{18}
Valence band effective density of state, N_V (cm^{-3})	1.8×10^{19}	1.8×10^{19}	1×10^{19}	1.8×10^{19}
Electronmobility, μ_n (cm^2 V^{-1} s^{-1})	20	100	2	30
Holemobility, μ_p (cm^2 V^{-1} s^{-1})	10	25	2	10
Shallow uniform donor doping density, N_D (cm^{-3})	1×10^{21}	1×10^{18}	0	0
Shallow uniform acceptor doping density, N_A (cm^{-3})	0	0	1×10^{15}	1×10^{18}
Defect density, N_t (cm^{-3})	1×10^{15}	1×10^{15}	1×10^{15}	1×10^{15}
Electron thermal velocity, V_e (cm s^{-1})	1×10^7	1×10^7	1×10^7	1×10^7
Hole thermal velocity, V_h (cm s^{-1})	1×10^7	1×10^7	1×10^7	1×10^7
Ref.	47	47 and 48	47	47

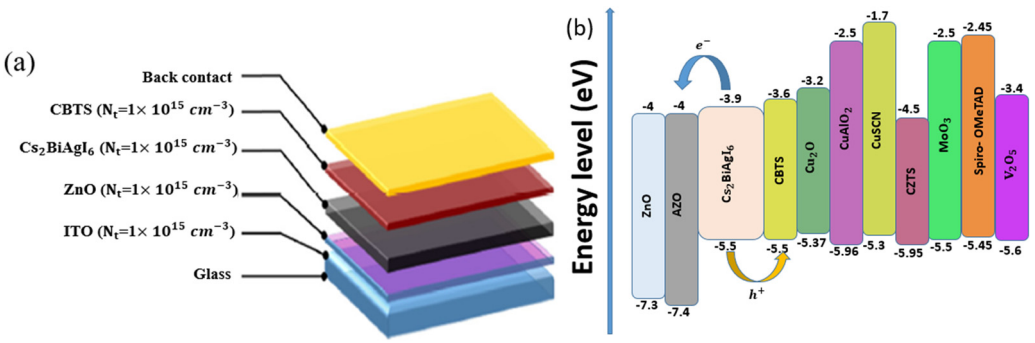

Fig. 1 (a) Device structure of the Cs_2AgBiI_6-DPSC. The defect densities of each layer (N_t) are shown in the parentheses. (b) Energy band alignment of ETLs, HTLs, and the DPPVK layer.

Table 2 Interface defect density parameters[47]

Interface parameter	ZnO/Cs_2BiAgI_6	Cs_2BiAgI_6/CBTS
Defect type	Neutral	Neutral
σ_n (cm^2)	1×10^{-17}	1×10^{-18}
σ_p (cm^2)	1×10^{-18}	1×10^{-19}
Distribution of energy	Single	Single
E_t–E_V	Above the VB maximum	Above the VB maximum
Energy level w.r.t. reference (eV)	0.6	0.6
N_t (cm^{-2})	1×10^{10}	1×10^{10}

$\sigma_{n,p}$: capture cross section for electron and hole; E_t: defect energy level; E_V: valence band minimum energy; N_t: interface defect density.

energy of 0.1 eV. These defects are electrically neutral and exhibit optimized capture cross sections for electrons and holes, with a value of 1×10^{-15} cm^2. The pre-factor for all the layers, denoted as A_α, is 1×10^5 (cm^{-1} $eV^{-0.5}$).[47] These values are determined ×using the following equation: $\alpha = A_\alpha(h\nu - E_g)^{0.5}$, where $h\nu$ represents the photon energy. Fig. 1(a) depicts a schematic representation of the Cs_2BiAgI_6-DPSC device configuration. The defect densities of each layer are specified in parentheses. Fig. 1(b) shows the energy band alignment for two ETLs, eight HTLs, and the DPPVK layer.

The validation of the model is confirmed through a comparison of the results obtained from Hossain *et al.*[47] with our model for the ITO/ZnO/Cs_2BiAgI_6 (800 nm)/CBTS/Au device. In Table 1, the material parameters for this device are presented. Table 2 shows the interface defect density parameters used in our simulation.

Fig. 2(a) shows our simulation of the current density–voltage curve of DPSC, ITO/ZnO/Cs_2BiAgI_6 (800 nm)/CBTS/Au, with the PV output parameters of V_{oc} of 1.0890 V, J_{sc} of 24.18 mA cm^{-2}, FF of 81.87%, and PCE of 21.56%, and Fig. 2(b) demonstrates the simulation of the EQE curve against the wavelength of the corresponding device. The EQE curve commences from 27.922% at 300 nm and reaches a peak of 99.807% at 360 nm. Then, it remains almost constant up to 600 nm and finally decreases to zero at 780 nm. Additionally, Fig. 2(c) shows the energy band alignment of this device.

Table 3 displays the comparison between the Hossain *et al.*[47] result and our simulated performance parameters of ITO/ZnO/Cs_2BiAgI_6 (800 nm)/CBTS/Au.

In this step, we examined AZO ETL and various HTLs to enhance efficiency. It is presumed that the N_D (cm^{-3}) and N_t (cm^{-3}) values of AZO ETL are the same as those of ZnO.

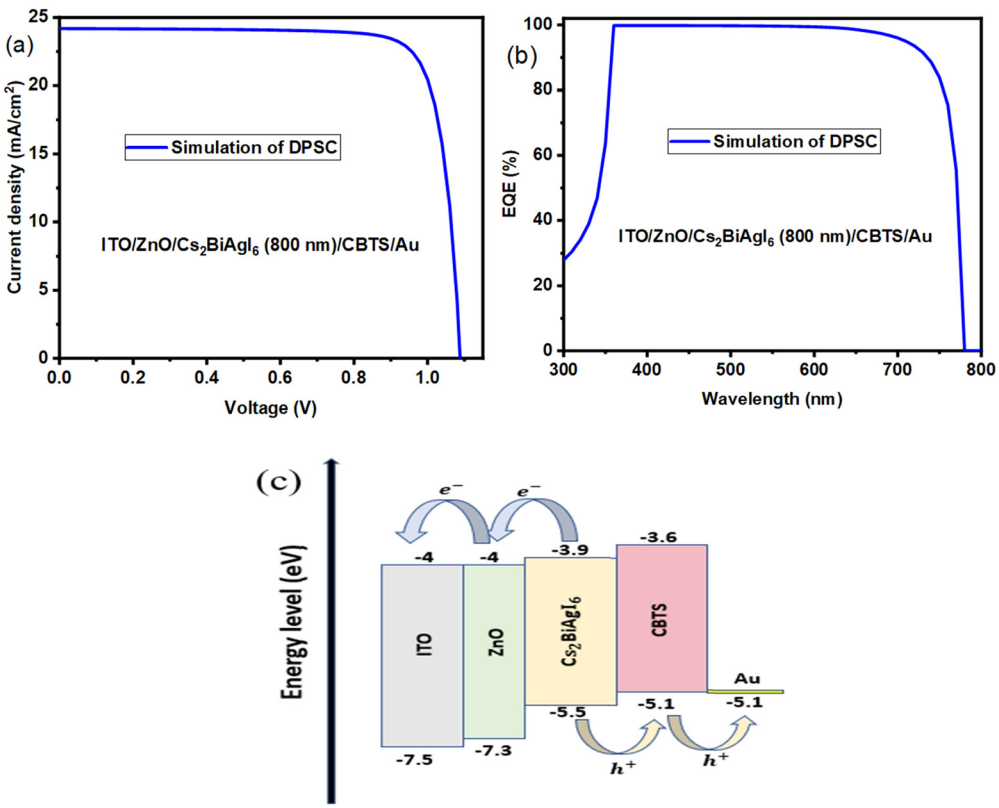

Fig. 2 Simulation results for the (a) current density–voltage (*J*–*V*) curve, (b) external quantum efficiency (EQE) curve, and (c) energy band alignment of the ITO/ZnO/Cs_2BiAgI_6 (800 nm)/CBTS/Au device.[47]

Table 3 Comparison of the results of Hossain *et al.*[47] with our simulation of performance parameters for ITO/ZnO/Cs_2BiAgI_6 (800 nm)/CBTS/Au

PV parameters	V_{oc} (V)	J_{sc} (mA cm^{-2})	FF (%)	PCE (%)
Hossain *et al.*[47]	1.085	23.76	83.78	21.59
Simulation	1.089	24.18	81.87	21.56

V_{oc} (open-circuit voltage), J_{sc} (short-circuit current density), FF (fill factor), and PCE (power conversion efficiency).

It is assumed that the thickness of all HTLs is the same as the value of CBTS, and the values of N_A (cm^{-3}) and N_t (cm^{-3}) are equal to those of CBTS. Table 4 presents the input material parameters of AZO ETL and different HTLs used in our simulation.

2.2.1. Influence of various ETLs and HTLs. Herein, we explored a DPSC based on Cs_2BiAgI_6 with an initial configuration using two kinds of ETLs, eight kinds of HTLs, and Au as a back contact. For this study, we used a total of eight HTLs comprising Cu_2O, CuSCN, V_2O_5, Spiro-OMeTAD, MoO_3, $CuAlO_2$, CZTS, CBTS, and two ETLs (ZnO and ZnO/AZO) to compare the PV performance for these 16 configurations. During the performance evaluation, the appropriate Cs_2BiAgI_6 absorber seems to be with HTLs, such as CBTS, $CuAlO_2$, CZTS, MoO_3, and V_2O_5 (Fig. 3). Compared with these HTLs, the performance of Cu_2O, CuSCN, and Spiro-OMeTAD was reduced when paired with any of the ETLs. As a p-type layer, the HTL must be thinner than the n-type ETL to avoid recombination and allow for the fast exchange of sufficient charge carriers in the structure. In Fig. 3(a), each of ZnO or ZnO/AZO ETLs and V_2O_5 HTL showed the highest V_{oc} of 1.894–1.897 V, while CuSCN HTL showed the lowest V_{oc} of 1.0845–1.0847 V. The J_{sc} of the CBTS HTL was the highest, 24.18 mA cm^{-2}, among all of the studied HTLs, as illustrated in Fig. 3(b). ZnO/AZO ETL and CuSCN HTL showed the lowest J_{sc} of 24.16 mA cm^{-2}. Fig. 3(c) depicts that the V_2O_5 HTL had the highest FF of 81.91–81.93%, whereas the Spiro-OMeTAD HTL demonstrated the lowest FF of 81.19–81.21% for all the studied transport layers. Fig. 3(d) illustrates the lowest performance of CuSCN HTL, 21.34–21.35%, while V_2O_5 HTL illustrates the highest performance of 21.58–21.59%. The V_2O_5 is characterized by several features, including excellent climate stability and strong optical and electrical properties. The V_2O_5 film can be fabricated by applying an inexpensive and simple spin-coating technique;[57] additionally, it was used as an HTL and interlayer between the perovskite absorber/HTL interface to achieve high solar cell performance.[58–61] V_2O_5 layer has a direct band gap of about 2.20 eV with good thermal stability, optical absorption coefficient, and long-term performance and has been recently put into the high priority production list because of its low environmental impact and low-cost fabrication techniques.[62] Furthermore, V_2O_5 nanoparticles were suitable for the modification of PEDOT:PSS (poly(3,4-ethylenedioxythiophene) polystyrene sulfonate owing to their high stability in acid, good dispersibility in polar solvents, and excellent photoelectric properties, the). Therefore, the conductivity of the resulting anode interfacial layer (AIL) improved. It exhibited different AIL conductivities, where the V_2O_5:PEDOT:PSS had the highest conductivity owing to the V_2O_5 nanoparticles filling the pinholes, exposing more PEDOT:PSS chains to the surface core–shell structure.[63]

For wiser decision of results, Fig. 3 illustrates the PV output parameters (V_{oc} (V), J_{sc} (mA cm^{-2}), FF (%), and PCE (%)) of the device of ITO/ETLs/Cs_2BiAgI_6 (800 nm)/HTLs/Au, for two ETL and eight HTL materials, as contour mapping plots.

Table S1 (ESI†) presents the PV output parameters of 16 devices for two ETLs and eight HTLs of Cs_2BiAgI_6-DPSC, and ITO/ETLs/Cs_2BiAgI_6 (800 nm)/HTLs/Au. Fig. S1a–d (ESI†) displays the *J*–*V* and EQE curves with the corresponding ETLs (a) and (b) ZnO/AZO and (c) and (d) ZnO for the device of ITO/ETLs/Cs_2BiAgI_6 (800 nm)/HTLs/Au. The eight HTLs are shown in the inset of Fig. S1a–d (ESI†).

According to Table S1 (ESI†) and Fig. 3, it can be concluded that the Cs_2BiAgI_6-DPSC with ETL (ZnO/AZO) and HTL (V_2O_5) has the maximum PCE, attaining 21.59%, together with a V_{oc} of 1.0897 V, J_{sc} of 24.17 mA cm^{-2}, and FF of 81.93%. We employ an ultra-thin layer of AZO (10 nm) on a ZnO, ITO/ZnO/AZO/Cs_2BiAgI_6 (800 nm)/V_2O_5/Au device in our simulation. By incorporating an AZO UTL layer, the extraction of electrons is improved at the interface, resulting in efficient carrier extraction, minimal leakage loss,[64] and reduced energy loss.[65] Additionally, it enhances the alignment of energy levels, facilitates electron transport, and enhances resistance to recombination.[66] A bilayer ETL can be designed to have superior film quality, lower trap

Table 4 Input material parameters of AZO (ETL) and different HTLs used in our simulation

	ETL				HTL			
Material parameters	AZO	Cu_2O	$CuAlO_2$	CuSCN	CZTS	MoO_3	Spiro-OMeTAD	V_2O_5
Thickness (nm)	10	100	100	100	100	100	100	100
E_g (eV)	3.4	2.17	3.46	3.6	1.45	3	3	2.2
χ (eV)	4	3.2	2.5	1.7	4.5	2.5	2.45	3.4
ε_r	9	7.1	60	10	9	12.5	3	10
N_C (cm^{-3})	2×10^{18}	2.02×10^{17}	2.2×10^{18}	2.2×10^{19}	2.2×10^{18}	2.2×10^{18}	2.2×10^{18}	9.2×10^{17}
N_V (cm^{-3})	1.8×10^{19}	1×10^{19}	1.8×10^{19}	1.8×10^{18}	1.8×10^{19}	1.8×10^{19}	1.8×10^{19}	5×10^{18}
μ_n (cm^2 V^{-1} s^{-1})	150	200	2	100	60	25	2×10^{-4}	3.2×10^{2}
μ_p (cm^2 V^{-1} s^{-1})	25	80	8.6	25	20	100	2×10^{-4}	4×10^{1}
N_D (cm^{-3})	1×10^{18}	0	0	0	0	0	0	0
N_A (cm^{-3})	0	1×10^{18}	1×10^{18}	1×10^{18}	1×10^{18}	1×10^{18}	1×10^{18}	1×10^{18}
N_t (cm^{-3})	1×10^{15}	1×10^{15}	1×10^{15}	1×10^{15}	1×10^{15}	1×10^{15}	1×10^{15}	1×10^{15}
Ref.	49–51	52	37	47	53	51	54 and 55	56

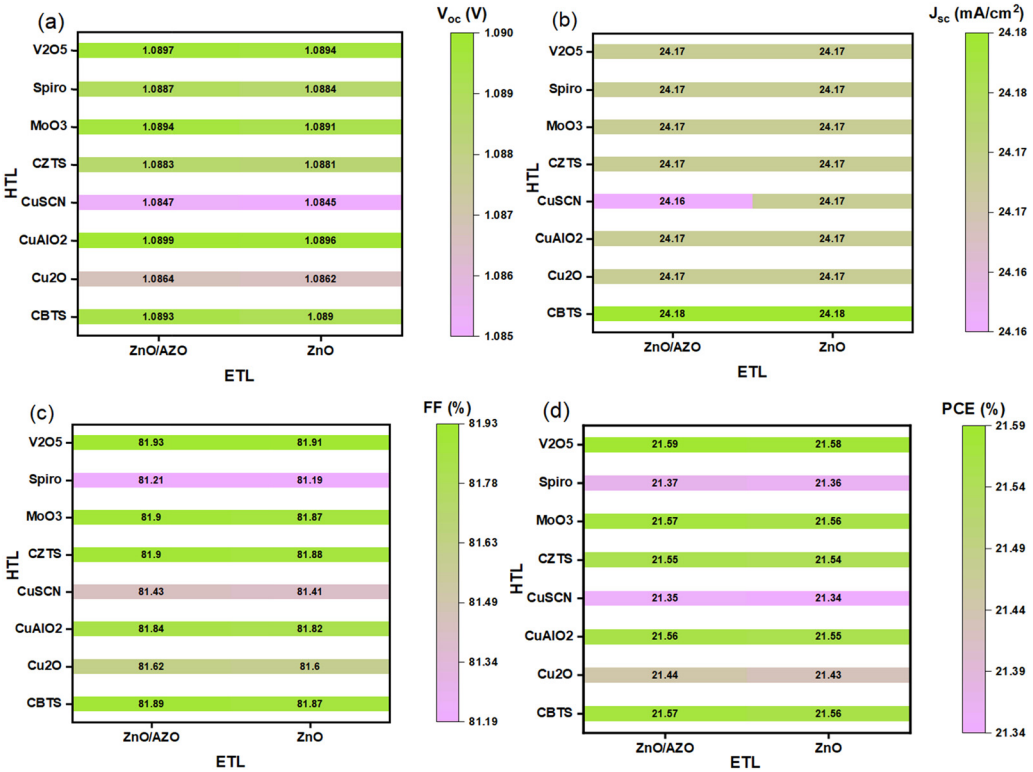

Fig. 3 Photovoltaic output parameters of (a) V_{oc} (V), (b) J_{sc} (mA cm^{-2}), (c) FF (%), and (d) PCE (%). Contour mapping plots of the device of ITO/ETLs/Cs_2BiAgI_6 (800 nm)/HTLs/Au for two ETLs and eight HTLs with different materials.

density, and decreased charge accumulation at the ETL/perovskite interface in the devices. The bilayer structure also displays a uniform, smooth surface with fewer defects, which enhances charge extraction at the ETL/DPPVK layer junction compared to a single layer.[67] This strategy presents a promising and efficient approach for producing cost-effective, high-performance, and reliable planar DPSCs.[40]

Fig. 4(a) presents the current density–voltage (J–V) curve, and Fig. 4(b) illustrates the external quantum efficiency (EQE) curve of ITO/ZnO/AZO/Cs_2BiAgI_6 (800 nm)/V_2O_5/Au device. The EQE curve originates from 27.782% at 300 nm and reaches a peak of 99.711% at 360 nm. Then, it remains constant until 600 nm and finally decreases to zero at 780 nm. Table S2 (ESI†) shows the interfacial defect density parameters of ITO/ZnO/AZO/Cs_2BiAgI_6 (800 nm)/V_2O_5/Au device.

3. Results and discussion

3.1. Energy band alignment

The energy band alignment between the passivation layer and the DPSC plays a crucial role in determining the performance of the DPSCs. The conduction band (CB) alignment between the passivation layer and the DPSC is particularly important for

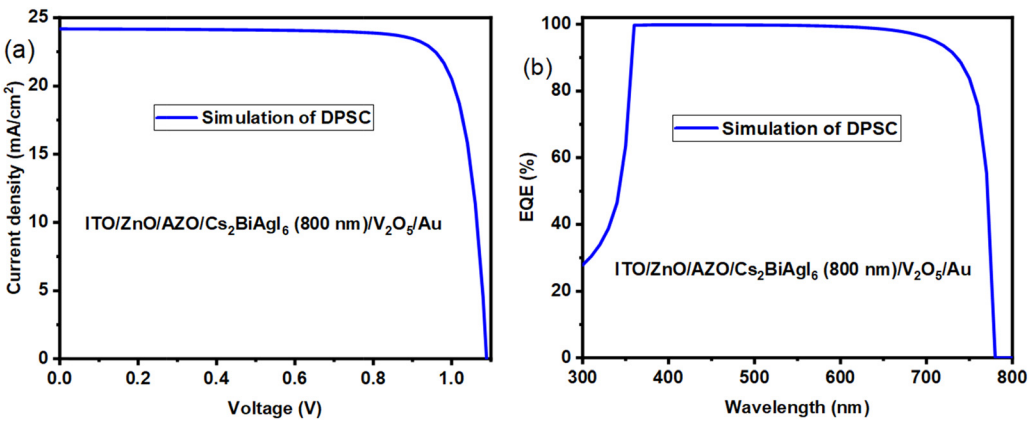

Fig. 4 (a) J–V curve and (b) EQE curve for ITO/ZnO/AZO/Cs_2BiAgI_6 (800 nm)/V_2O_5/Au device.

efficient electron extraction from double perovskite material. It is necessary to have a minimal offset between the CB of the passivation layer and the CB of the DPSC to ensure effective electron extraction. However, the valence band (VB) alignment between the passivation layer and the DPSC is important for blocking the movement of holes. A considerable difference in the VBs is required to prevent holes from migrating towards the ETL and causing recombination. Similarly, proper alignment between the valence band of the HTL and the double perovskite material is crucial for facilitating hole separation. Additionally, a significant offset in the conduction bands of the HTL and DPSC is necessary to prevent electron migration towards the HTL and minimize recombination. To achieve optimal band alignment in DPSCs, a minimal offset at the CB and a maximal offset at the VB between the double perovskite and the ETL are essential, enabling electron flow while blocking hole transmission.[68] Similarly, minimal VBO (valence band offset) and maximal CBO (conduction band offset) affect HTL and double perovskite characteristics. These offsets enable seamless transmission of holes from the absorber to the HTL while impeding electron mobility. Fig. S2 (ESI†) depicts the energy band alignment of the Cs_2BiAgI_6-DPSCs, while Table 5 presents the VBO and CBO assessed by the respective layers. The VBO and CBO values are calculated based on the material's electron affinity (χ) and energy band gap (E_g), as follows:

$$\mathrm{CBO} = \chi_{\mathrm{DPPVK}} - \chi_{\mathrm{CTL}}, \quad (5)$$

$$\mathrm{VBO} = (\chi_{\mathrm{CTL}} + E_{\mathrm{g,CTL}}) - (\chi_{\mathrm{DPPVK}} + E_{\mathrm{g,DPPVK}}). \quad (6)$$

The implementation of an interlayer (IL) is noted to modify the arrangement of energy levels within the films and hinder ion migration. The alignment of interface energy levels significantly affects the rate at which electrons are injected, particularly between the DPPVK layer and the ETL. The presence of an energy barrier at the interfaces results in the recombination of charge carriers, thereby restricting the efficiency of charge transfer. Conversely, the lack of an energy barrier across the interface promotes efficient charge transfer and injection, leading to reduced recombination rates. The addition of an AZO IL, which acts as a passivation layer at the interface of the DPPVK layer and the ETL, improves electron transport through the interface and could potentially reduce interface charge recombination.

Table 5 CBO and VBO at interfaces

Interface	CBO (eV)	VBO (eV)
Double perovskite/ETL		
Cs_2BiAgI_6/ZnO	−0.1	1.8
Double perovskite/passivation		
Cs_2BiAgI_6/AZO	−0.1	1.9
Passivation/ETL		
AZO/ZnO	0	0.1
Double perovskite/HTL		
Cs_2BiAgI_6/CBTS	0.3	0
Cs_2BiAgI_6/Cu_2O	0.7	−0.13
Cs_2BiAgI_6/$CuAlO_2$	1.4	0.46
Cs_2BiAgI_6/CuSCN	2.2	−0.2
Cs_2BiAgI_6/CZTS	−0.6	0.45
Cs_2BiAgI_6/MoO_3	1.4	0
Cs_2BiAgI_6/Spiro	1.45	−0.05
Cs_2BiAgI_6/V_2O_5	0.5	0.1

3.2. Influence of total generation and recombination rate

Owing to the light incident on the double perovskite solar cell, Fig. 5a–d illustrates the generation and recombination rates for different ETLs. Electron transfers from valence to the conduction band, leaving a hole. The release of electrons and holes contributes to carrier generation. The SCAPS-1D software utilizes the incident photon flux $N_{\mathrm{phot}}(\lambda, x)$ to determine the creation of electron–hole pairs $G(\lambda, x)$. By analyzing this photon flux at different positions and wavelengths, the value of $G(\lambda, x)$ can be calculated as follows:

$$G(\lambda, x) = \alpha(\lambda, x) \cdot N_{\mathrm{phot}}(\lambda, x), \quad (7)$$

where $\alpha(\lambda, x)$ is the absorption coefficient and $N_{\mathrm{phot}}(\lambda, x)$ is the photon incident number. Recombination is the opposite of generation, involving the pairing and annihilation of electrons and holes in the conduction band. The recombination rate of a solar cell is determined by the lifespan and density of the charge carriers. Initially, electron–hole recombination is reduced owing to defect states in the absorber layer. Subsequently, the creation of energy states affects the electron–hole recombination profile in the structure of the solar cell. Recombination rates alter owing to defects, as shown in Fig. 5b and d.[69] Recombination rate in ZnO/AZO is a little smaller than that of ZnO for V_2O_5, as illustrated in Fig. 5b and d.

3.3. Influence of the thickness of the double perovskite absorber (DPPVK) layer on the Cs_2BiAgI_6-DPSC performance

Herein, we determine the optimum parameters for the ITO (500 nm)/ZnO (50 nm)/AZO (10 nm)/Cs_2BiAgI_6 (800 nm)/V_2O_5 (100 nm)/Au device. The impact of varying the thickness of the double perovskite absorber (DPPVK) layer on the cell parameters was calculated. The DPPVK layer thickness ranged from 50 to 1000 nm in 20 increments, with the parameters shown in Fig. 6. In Fig. 6(a), the current density–voltage curves for DPPVK layers from 50 to 1000 nm in 20 steps are shown. As depicted in Fig. 6(b), increasing the DPPVK layer thickness from 50 to 1000 nm in 20 steps, up to 650 nm, boosts EQE; after that, it rises slightly. This increase is due to more charge carriers resulting from better light absorption.[70] Fig. 6(c) illustrates the device's performance parameters in proportion to the thickness of the DPPVK layer changing from 50 to 1000 nm in 20 steps. The thickness of the DPPVK layer significantly influences the quality and performance of the DPSCs.

In accordance with Fig. 6(c), the V_{oc} and FF of the DPPVK layer diminish as the thickness of the layer augments. This is because the excitons generated from photon absorption are unable to overcome the barrier potential of the depletion layer, resulting in a higher recombination rate of charge carriers and an increased reverse saturation current, which ultimately leads to a decrease in V_{oc}.

Increasing the thickness of the DPPVK layer also enhances photon absorption, resulting in the production of more excitons, which, in turn, increases the J_{sc} and the overall PCE of the DPSC.[71] However, further increasing the thickness leads to

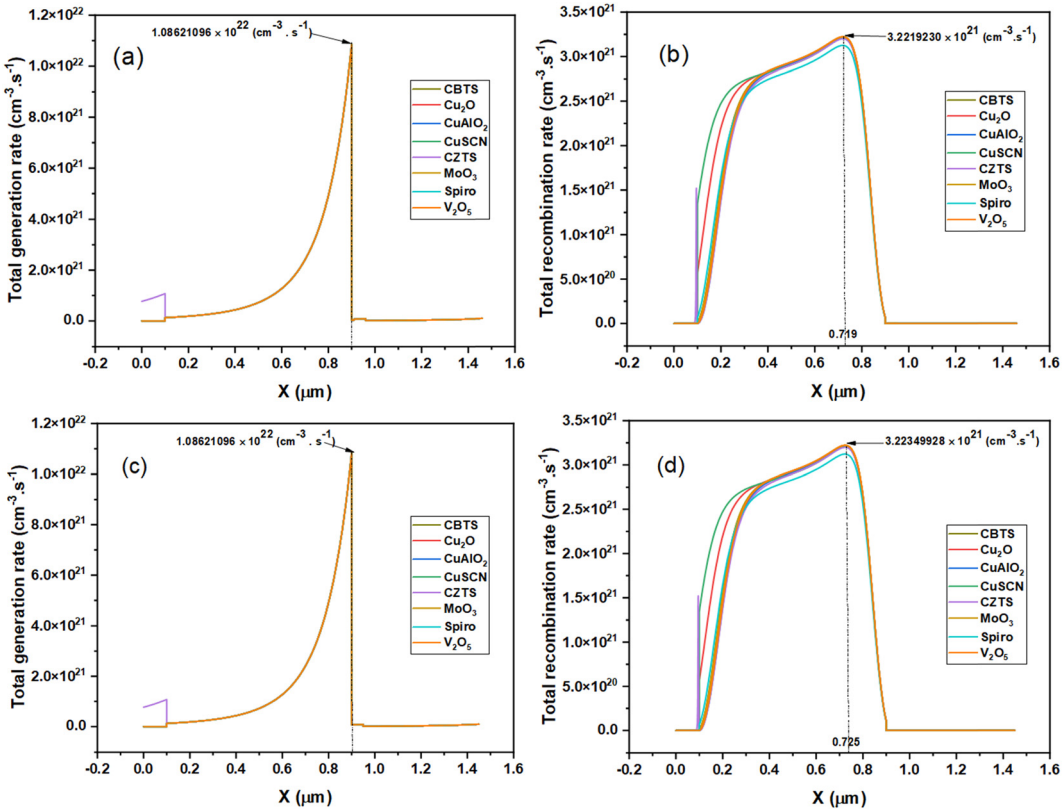

Fig. 5 Total generation and recombination rate of (a) and (b) ZnO/AZO and (c) and (d) ZnO ETLs.

higher series resistance, which introduces more defects and increases the recombination rate, thereby reducing the FF.[72,73]

Therefore, when determining the optimal absorber thickness, it is crucial to consider all factors, including V_{oc}, J_{sc}, FF, and PCE. Experimental studies have demonstrated that the performance of DPSCs is heavily influenced by the morphology of the DPPVK layer, which directly affects the photogenerated lifetime and diffusion length.[74,75]

Fig. 6(c) demonstrates the performance parameters to Cs_2BiAgI_6 thickness (50–1000 nm in 20 steps). The optimal value occurs at a thickness of 650 nm, with the corresponding PV output parameters of V_{oc} at 1.1005 V, J_{sc} at 23.78 mA cm^{-2}, FF of 82.78%, and PCE of 21.67%. The V_{oc} decreases from 1.2101 V to 1.0790 V, J_{sc} increases from 9.85 mA cm^{-2} to 24.45 mA cm^{-2}, FF decreases from 85.07% to 80.76%, PCE increases from 10.14% to 21.67% at 650 nm, and then decreases to 21.31% at 1000 nm.

3.4. Influence of defect density in the double perovskite absorber (DPPVK) layer on the Cs_2BiAgI_6-DPSC performance

Various processes involving generation, recombination, and absorption occur within the DPPVK layer, directly affecting the quality of the layer and the defect density.[76] The efficiency of Cs_2BiAgI_6-DPSC is significantly affected by high defect densities in the DPPVK layer. These defects act as recombination centers, accelerating the recombination rate and shortening the lifespan of charge carriers, which ultimately leads to a decrease in device performance. In Cs_2BiAgI_6-DPSC, Shockley–Read–Hall (SRH) recombination is prevalent, and the trap-assisted SRH recombination model can be utilized to calculate the diffusion length.[77] The SRH recombination formula is represented as follows:

$$R_{SRH} = \frac{np - n_i^2}{\tau_{n,p}\left(p + n + 2n_i \cosh\left(\frac{E_i - E_t}{kT}\right)\right)}, \quad (8)$$

where R_{SRH} denotes SRH recombination; n and p denote the electron and hole concentration density, respectively; n_i denotes intrinsic density; $\tau_{n,p}$ denotes carrier lifetime; E_i denotes the intrinsic energy level; and E_t denotes trap energy level. Thus, we have

$$\tau_{n,p} = \frac{1}{\sigma_{n,p} \times N_t \times v_{th}}, \quad (9)$$

where $\sigma_{n,p}$ denotes the capture cross section of electrons and holes, v_{th} denotes the thermal velocity of charge carriers and N_t denotes the total bulk defect density of the DPPVK layer of the Cs_2BiAgI_6-DPSC. Moreover, the diffusion length L and the diffusion coefficient D are as follows:

$$L = \sqrt{D \times \tau_{n,p}}, \quad (10)$$

$$D = \frac{kT}{q}\mu_{n,p}, \quad (11)$$

where k, T, q, and $\mu_{n,p}$ represent Boltzmann's constant, temperature, charge carriers, and carrier mobility, respectively.

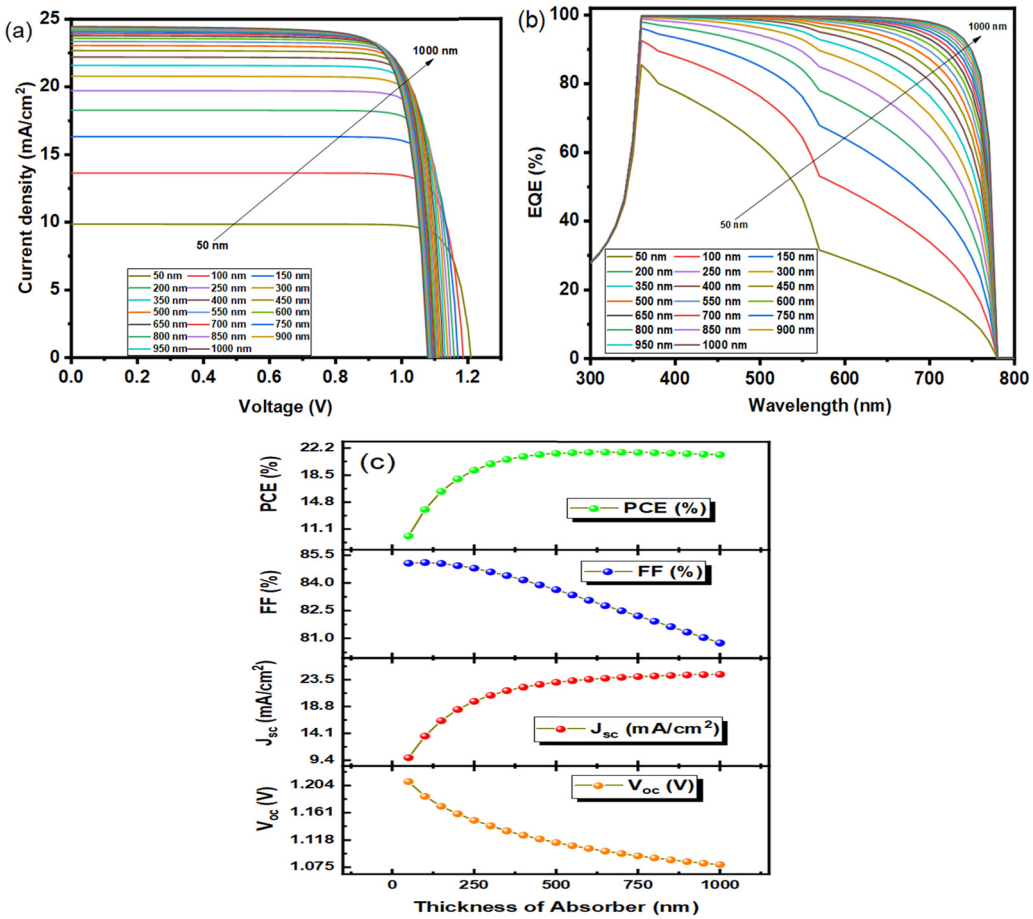

Fig. 6 (a) *J*–*V* curve, (b) EQE curve, and (c) performance parameters for different double perovskite absorber layer thicknesses ranging from 50 to 1000 nm in 20 steps.

The maximum distance that charge carriers can travel is determined by these equations, which are primarily influenced by the lifetimes of the carriers. In principle, the diffusion length of charge carriers depends mainly on their lifetimes. Furthermore, the defects found in the DPPVK layer serve as non-radiative SRH recombination centers.

Fig. 7a and b display the PV parameters against the defect density of the DPPVK layer, $N_{t,DPPVK}$, which ranges from 1×10^{13} cm^{-3} to 1×10^{17} cm^{-3}. As demonstrated in Fig. 7, the optimal value occurs at a defect density of 1×10^{13} cm^{-3}, with corresponding PV output parameters of V_{oc} at 1.321 V, J_{sc} at 23.83 mA cm^{-2}, FF of 84.50%, and PCE of 26.61%. As depicted in Fig. 7(a), V_{oc} decreases from 1.321 V to 0.8248 V as $N_{t,DPPVK}$ increases from 1×10^{13} cm^{-3} to 1×10^{17} cm^{-3}, and J_{sc} remains fixed at 23.83 mA cm^{-2} for both 1×10^{13} cm^{-3} and 1×10^{14} cm^{-3}, and 23.78 mA cm^{-2} at 1×10^{15} cm^{-3} and then decreases to 2.10 mA cm^{-2} at 1×10^{17} cm^{-3}. As illustrated in Fig. 7(b), FF decreases from 84.82% to 58.15% as $N_{t,DPPVK}$

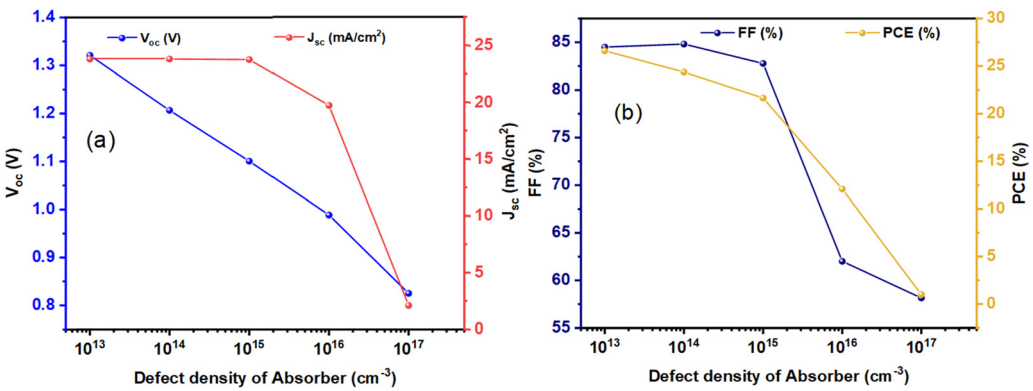

Fig. 7 (a) V_{oc} and J_{sc}, and (b) FF and PCE curves for Cs_2BiAgI_6-DPSC against defect density of absorber.

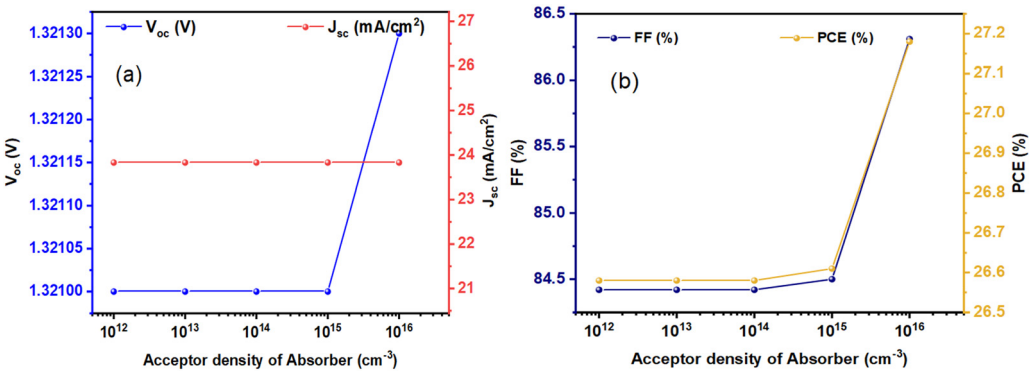

Fig. 8 (a) V_{oc} and J_{sc}, and (b) FF and PCE curves for Cs_2BiAgI_6-DPSC against acceptor density of absorber.

increases from 1×10^{14} cm^{-3} to 1×10^{17} cm^{-3}, and the PCE value is 24.39% at 1×10^{14} cm^{-3} and then decreases to 1.01% at 1×10^{17} cm^{-3}.

3.5. Influence of acceptor doping concentration in the absorber layer on the Cs_2BiAgI_6-DPSC performance

The performance of the Cs_2BiAgI_6-DPSC device is greatly affected by the doping in the DPPVK layer. To explore the effect of acceptor doping density on the Cs_2BiAgI_6-DPSC performance, we initially model the device performance by adjusting the acceptor doping concentration of the DPPVK layer ($N_{A,DPPVK}$) from 1×10^{12} cm^{-3} to 1×10^{16} cm^{-3}, as shown in Fig. 8.

Enhancing the density of dopants can increase the concentration of charge carriers, thus improving the performance of the Cs_2BiAgI_6-DPSC.[78,79] Nevertheless, excessively high levels of doping in the DPPVK layer can lead to reduced device performance, as high doping introduces more traps in the DPPVK layer that affect the mobility of charge carriers and result in increased recombination. Excessive doping densities also influence the semiconductor behavior of Cs_2BiAgI_6-DPSC, making it more metallic.

Fig. 8a and b show how the values of V_{oc}, J_{sc}, FF and PCE vary with the acceptor density of the DPPVK layer, which alters from 1×10^{12} cm^{-3} to 1×10^{16} cm^{-3}. Regarding the acceptor density in the DPPVK layer, the highest efficiency of 27.18% was achieved at an acceptor density of 1×10^{16} cm^{-3}, with the V_{oc} of 1.3213 V, J_{sc} of 23.83 mA cm^{-2}, and FF of 86.31%. As depicted in Fig. 8(a), V_{oc} is 1.321 V when $N_{A,DPPVK}$ increases from 1×10^{12} cm^{-3} to 1×10^{15} cm^{-3} and then increases to 1.3213 V at 1×10^{16} cm^{-3}, and J_{sc} remains unchanged at 23.83 mA cm^{-2} from 1×10^{12} cm^{-3} to 1×10^{16} cm^{-3}. As illustrated in Fig. 8(b), FF is 84.42% when $N_{A,DPPVK}$ increases from 1×10^{12} cm^{-3} and 1×10^{14} cm^{-3}, marginally increases up to 84.50% at 1×10^{15} cm^{-3}, and then increases to 86.31% at 1×10^{16} cm^{-3}; the PCE value is 26.58% as $N_{A,DPPVK}$ increases from 1×10^{12} cm^{-3} to 1×10^{14} cm^{-3}, increases to 26.61% at 1×10^{15} cm^{-3}, and increases to 27.18% at 1×10^{16} cm^{-3}.

3.6. Influence of defect density of V_2O_5-HTL on the Cs_2BiAgI_6-DPSC performance

Deficiencies in the V_2O_5 (HTL) film lead to an increase in defect density, causing a higher rate of electron and hole recombination within the film. Consequently, the PCE of Cs_2BiAgI_6-DPSC decreases.[80–82] Fig. 9 demonstrates the variation of V_{oc}, J_{sc}, FF and PCE for defect density of V_2O_5 and N_{t,V_2O_5}, altering from 1×10^{12} cm^{-3} to 1×10^{18} cm^{-3}. The optimum value increases at 1×10^{17} cm^{-3}, and the PV output parameters of Cs_2BiAgI_6-DPSC are V_{oc} of 1.3213 V, J_{sc} of 23.83 mA cm^{-2}, FF of 86.31%, and PCE of 27.18%. As shown in Fig. 9, V_{oc} is 1.3213 V when N_{t,V_2O_5} increases from 1×10^{12} cm^{-3} to 1×10^{17} cm^{-3} and then decreases to 1.3203 V at 1×10^{18} cm^{-3}, J_{sc} is 23.83 mA cm^{-2} when N_{t,V_2O_5} increases from 1×10^{12} cm^{-3} to 1×10^{18} cm^{-3}, FF is 86.31% when N_{t,V_2O_5} increases from 1×10^{12} cm^{-3} to 1×10^{18} cm^{-3}, and PCE value is 27.18% when N_{t,V_2O_5} increases from 1×10^{12} cm^{-3} to 1×10^{17} cm^{-3} and then moderately falls to 27.17%.

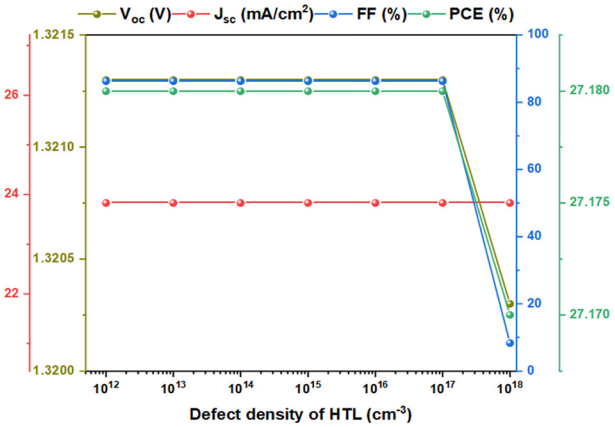

Fig. 9 PV output parameters for Cs_2BiAgI_6-DPSC against the defect density of V_2O_5-HTL.

3.7. Influence of conduction and valence band offset of V_2O_5-HTL based on the Cs_2BiAgI_6-DPSC performance

In the Cs_2BiAgI_6-DPSC, a comprehensive numerical analysis is conducted with device simulation to understand the device operation mechanism and develop an optimal layer configuration for enhanced efficiency. It is essential to examine the electronic properties of HTL and ETL, such as their electron affinity and band gap, when designing highly efficient solar cells. In this study, we aim to determine the ideal energy levels

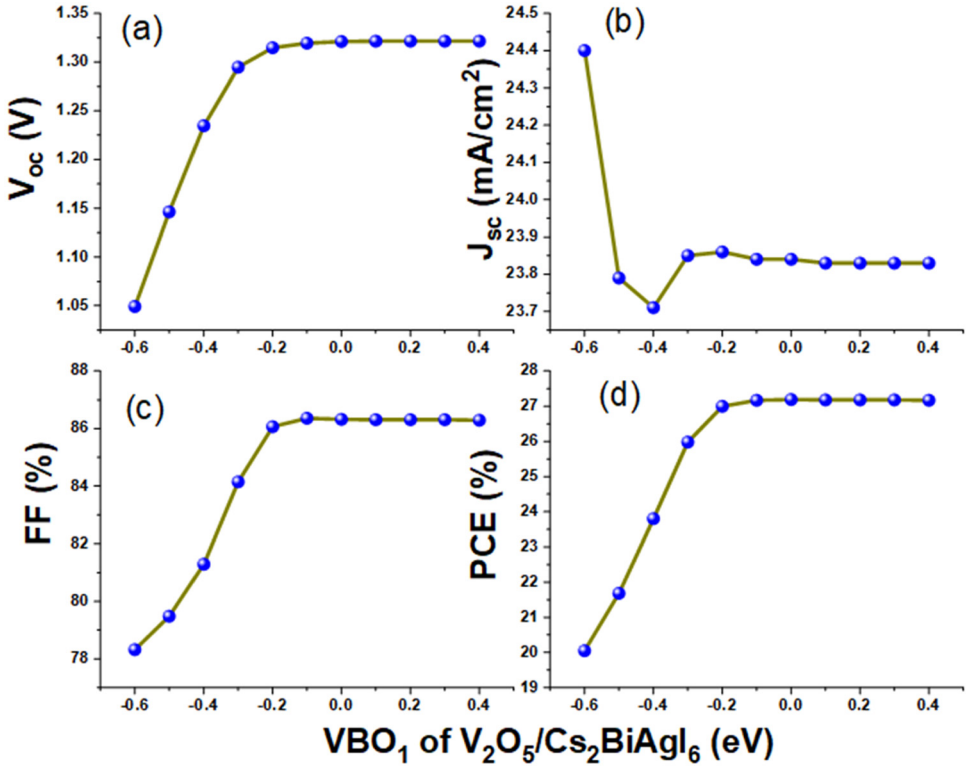

Fig. 10 (a)–(d) PV output parameters with the variation of VBO_1 of V_2O_5/Cs_2BiAgI_6 between −0.6 eV and +0.4 eV.

for efficient Cs_2BiAgI_6-DPSC design. To achieve this goal, careful selection of CBO_1 and VBO_1 is necessary. In this study, we investigate how modifying the affinities and band gaps of the V_2O_5 can lead to optimal values of CBO_1 and VBO_1. To achieve a higher V_{oc} and reduce recombination, CBO_1 or VBO_1 must be positive and below 0.3 eV. Negative CBO_1 or VBO_1 values increase electron and hole accumulation, causing more recombination and lower charge output.[83] A positive CBO_1 or VBO_1 restricts electron movement, while a negative one facilitates it.[83] The charge polarity of CBO_1 and VBO_1 is determined by the barrier height of the charge carriers generated by light, as follows:

$$CBO_1 = \chi_{HTL} - \chi_{DPPVK}, \quad (12)$$

$$VBO_1 = (\chi_{HTL} + E_{g,HTL}) - (\chi_{DPPVK} + E_{g,DPPVK}). \quad (13)$$

The electron affinity of HTL changes from 1.5 eV to 2.5 eV, and VBO_1 is altered from −0.6 eV to +0.4 eV. Therefore, according to Table S3 (ESI†), when the energy band gap of HTL is concerned, the optimum value increases at 2.1 eV or VBO_1 is 0.0 eV, with the PV output parameters obtained as V_{oc} of 1.321 V, J_{sc} of 23.84 mA cm^{-2}, FF of 86.32%, and PCE of 27.19%. Fig. S3(a) (ESI†) shows the current density-volt xage curve, Fig. S3(b) (ESI†) illustrates the energy band diagram, and the inset of the figures demonstrates the variation of the energy level of V_2O_5-HTL based *versus* VBO_1 values. Fig. 10a–d illustrates the PV output parameters with a variation of VBO_1 between −0.6 eV and +0.4 eV. According to our calculations, there is no change in CBO_1, see Table S4 (ESI†).

3.8. Influence of defect density of AZO UTL on the Cs_2BiAgI_6-DPSC performance

Defects in the AZO UTL film lead to more electron–hole recombination. Consequently, the PCE of the Cs_2BiAgI_6-DPSC decreases.[84,85] Fig. 11 shows the variation of V_{oc}, J_{sc}, FF and PCE for defect density of AZO UTL, $N_{t,AZO}$, increasing from 1 × 10^{12} cm^{-3} to 1 × 10^{19} cm^{-3}. The optimum value increases at 1 × 10^{16} cm^{-3}, and the PV output parameters of Cs_2BiAgI_6-DPSC are V_{oc} of 1.321 V, J_{sc} of 23.84 mA cm^{-2}, FF of 86.32%, and PCE of 27.19%. As depicted in Fig. 11, V_{oc} is 1.321 V when $N_{t,AZO}$ increases from 1 × 10^{12} cm^{-3} to 1 × 10^{16} cm^{-3}, slightly

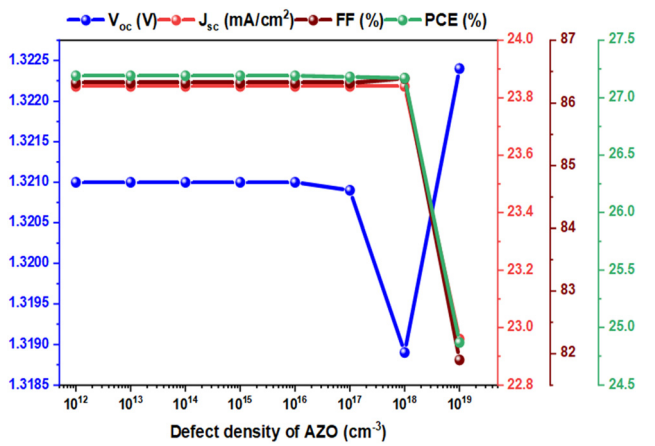

Fig. 11 PV output parameters for Cs_2BiAgI_6-DPSC against the defect density of AZO UTL.

decreases to 1.3189 V at 1×10^{18} cm^{-3}, and then increases to 1.3224 V at 1×10^{19} cm^{-3}. J_{sc} is 23.84 mA cm^{-2} when $N_{t,AZO}$ increases from 1×10^{12} cm^{-3} to 1×10^{18} cm^{-3} and then decreases to 22.96 mA cm^{-2} at 1×10^{19} cm^{-3}. FF is 86.32% as $N_{t,AZO}$ increases from 1×10^{12} cm^{-3} to 1×10^{17} cm^{-3}, increases to 86.39% at 1×10^{18} cm^{-3}, and then decreases to 81.90% at 1×10^{19} cm^{-3}. PCE value is 27.19% as $N_{t,AZO}$ increases from 1×10^{12} cm^{-3} to 1×10^{16} cm^{-3}; to some extent, increases to 27.18% at 1×10^{17} cm^{-3} and 27.17% at 1×10^{18} cm^{-3}; and then decreases to 24.87% at 1×10^{19} cm^{-3}.

3.9. Influence of valence and conduction band offset of AZO UTL on the Cs_2BiAgI_6-DPSC performance

To determine the optimal energy level, it is crucial to carefully select the values of CBO_2 and VBO_2 for the AZO UTL.[83] The barrier heights (CBO_2 and VBO_2) can be influenced by photo-generated charge carriers, either positive or negative, as follows:

$$CBO_2 = \chi_{DPPVK} - \chi_{AZO}, \quad (14)$$

$$VBO_2 = (\chi_{DPPVK} + E_{g,DPPVK}) - (\chi_{AZO} + E_{g,AZO}). \quad (15)$$

Eqn (14) represents the electron affinity of the DPPVK layer (χ_{DPPVK}) and the electron affinity of the AZO UTL (χ_{AZO}). Eqn (15) presents the band gap energy of the DPPVK layer ($E_{g,DPPVK}$) and the band gap energy of the AZO UTL ($E_{g,AZO}$).

There is no change in VBO_2; see Table S5 (ESI†). In Table S6 (ESI†), PV output parameters are shown, the electron affinity of AZO ranges from 3.5 eV to 4.1 eV, and the CBO_2 values change from +0.4 eV to −0.2 eV. Fig. S4(a) (ESI†) shows the plots of current density–voltage curves for different values of CBO_2, while Fig. S4(b) (ESI†) illustrates the energy band diagram with various CBO_2 values as indicated by different colors. Fig. 12a–d presents the PV output parameters corresponding to several CBO_2 values. The optimal value for the DPPVK layer/AZO UTL interface occurs when the electron affinity of AZO UTL is 3.9 eV. The optimum value increases at CBO_2 = +0.0 eV because it has better energy alignment and an efficiency of 27.20%, while the PV output parameters of Cs_2BiAgI_6-DPSC are as follows: V_{oc} of 1.3221 V, J_{sc} of 23.84 mA cm^{-2}, FF of 86.29%, and PCE of 27.20%.

3.10. Influence of defect density of ZnO layer on the Cs_2BiAgI_6-DPSC performance

Because of ZnO layer flaws, the defect density increases, leading to more charge carrier recombination. This leads to a decrease in the PCE of the Cs_2BiAgI_6-DPSC.[86] As depicted in Fig. 13, the defect density of ZnO changes from 1×10^{12} cm^{-3} to 1×10^{18} cm^{-3}. As illustrated in Fig. 13, V_{oc} is a constant value at 1.3222 V as $N_{t,ZnO}$ increases from 1×10^{12} cm^{-3} to 1×10^{17} cm^{-3}, and then marginally decreases to 1.3220 V at 1×10^{18} cm^{-3}. J_{sc} remains fixed at 23.84 mA cm^{-2} as $N_{t,ZnO}$ increases from 1×10^{12} cm^{-3} to 1×10^{16} cm^{-3} and slightly decreases to 23.79 mA cm^{-2} at 1×10^{18} cm^{-3}. FF value is 86.28% when $N_{t,ZnO}$ increases from 1×10^{12} cm^{-3} to 1×10^{17} cm^{-3} and

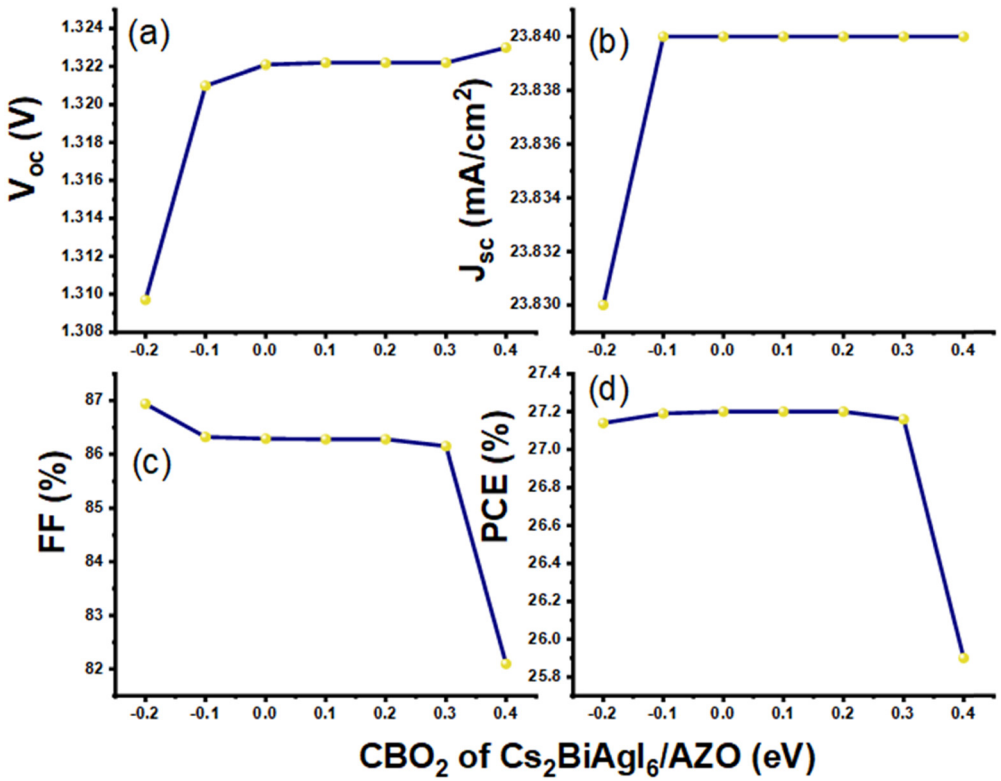

Fig. 12 (a)–(d) PV output parameters with the variation of CBO_2 of Cs_2BiAgI_6/AZO UTL between −0.2 eV and +0.4 eV.

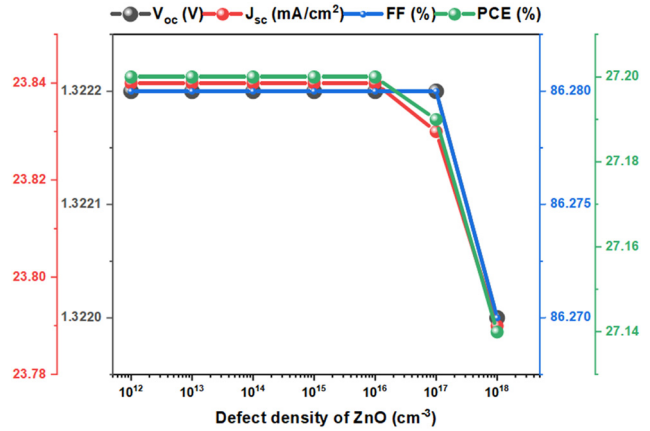

Fig. 13 PV output parameters for Cs_2BiAgI_6-DPSC against the defect density of the ZnO layer.

then fairly decreases to 86.27% at 1×10^{18} cm^{-3}. PCE value is 27.20% when $N_{t,ZnO}$ increases from 1×10^{12} cm^{-3} to 1×10^{16} cm^{-3} and then scarcely decreases to 27.14% at 1×10^{18} cm^{-3}.

3.11. Influence of interfacial defect density on the Cs_2BiAgI_6-DPSC performance

To optimize the efficiency of DPSCs, the quality of the junction plays a crucial role in determining the capabilities of the interface. Our focus in this stage was on adjusting the defect densities at the interface to emphasize the significance of interface quality and recombination rate in actual Cs_2BiAgI_6-DPSCs. Interactions between double perovskites and transport materials often contain multiple defect states, highlighting the importance of the quality of these interfaces for the PCE of Cs_2BiAgI_6-DPSC. Notably, the interface defect density near the illuminated side exerts a more pronounced influence on Cs_2BiAgI_6-DPSC performance compared to the back interface.[87] With an increase in these defects, additional trap levels emerge at the interface, consequently elevating the resistance of Cs_2BiAgI_6-DPSC. The heightened resistances impede the movement of charge carriers, promoting recombination and ultimately diminishing the PCE of DPSC.[88]

Herein, there are three categories of interface defect densities: the first one is between the HTL and DPPVK layer, the second one is between AZO UTL and DPPVK layer, and the third one is between AZO UTL and ZnO layer.

In Fig. 14(a), it is demonstrated that the optimum value for the interface defect density (N_{it}) of the HTL/DPPVK layer (N_{it} changes from 1×10^5 cm^{-2} to 1×10^{15} cm^{-2}) is 1×10^{10} cm^{-2}; the PV output parameters are as follows: V_{oc} of 1.3221 V, J_{sc} of 23.84 mA cm^{-2}, FF of 86.28%, and PCE of 27.20%. Regarding HTL/DPPVK interface defect density, V_{oc} is 1.3222 V from 1×10^5 cm^{-2} to 1×10^9 cm^{-2} and then decreases to 1.1852 V at 1×10^{15} cm^{-2}. The parameter of J_{sc} remains constant, 23.84 mA cm^{-2}, as N_{it} increases from 1×10^5 cm^{-2} to 1×10^{12} cm^{-2} and then slightly decreases to 23.72 mA cm^{-2} at 1×10^{15} cm^{-2}. The FF remains constant at 86.28% from 1×10^5 cm^{-2} to 1×10^{10} cm^{-2}, increases to 89.36% at 1×10^{14} cm^{-2}, and then decreases to 88.47% at 1×10^{15} cm^{-2}. The PCE

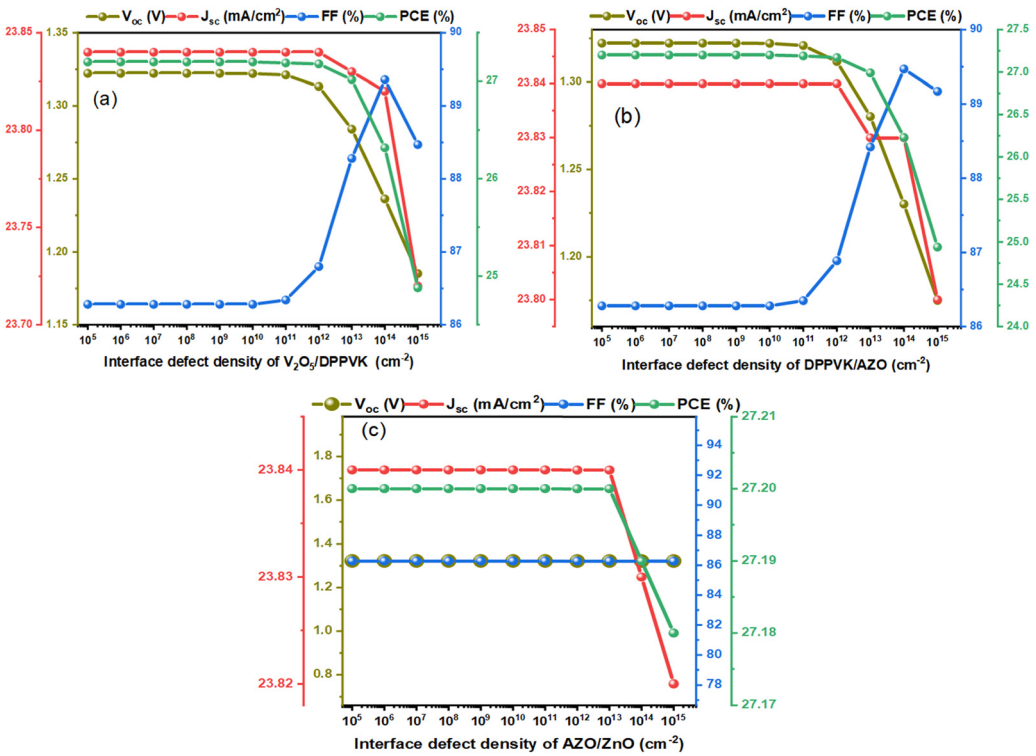

Fig. 14 PV output parameters for interface defect density of (a) V_2O_5 layer/DPPVK layer, (b) DPPVK layer/AZO UTL, and (c) AZO UTL/ZnO layer of Cs_2BiAgI_6-DPSC.

remains immutable, 27.20%, from 1×10^5 cm^{-2} to 1×10^{10} cm^{-2} and then decreases to 24.88% at 1×10^{15} cm^{-2}.

In Fig. 14(b), the DPPVK layer/AZO UTL interface defect density is changed from 1×10^5 cm^{-2} to 1×10^{15} cm^{-2}. V_{oc} is fixed at 1.3222 V as N_{it} increases from 1×10^5 cm^{-2} to 1×10^9 cm^{-2} and then decreases to 1.1750 V at 1×10^{15} cm^{-2}. J_{sc} remains unchanged at 23.84 mA cm^{-2} as N_{it} enhances between 1×10^5 cm^{-2} and 1×10^{12} cm^{-2}. At this point, it marginally dwindles to 23.83 mA cm^{-2} at both 1×10^{13} cm^{-2} and 1×10^{14} cm^{-2} and then decreases to 23.80 mA cm^{-2} at 1×10^{15} cm^{-2}. The FF value is fixed at 86.28% when N_{it} increases from 1×10^5 cm^{-2} to 1×10^{10} cm^{-2} and subsequently increases to 89.17% at 1×10^{15} cm^{-2}. The PCE value is constant at 27.20% as N_{it} increases from 1×10^5 cm^{-2} to 1×10^{10} cm^{-2} and subsequently decreases to 24.94% at 1×10^{15} cm^{-2}. Concerning the optimal value of this interface defect density, it occurs at 1×10^{10} cm^{-2}, with the following PV output parameters: V_{oc} of 1.3221 V, J_{sc} of 23.84 mA cm^{-2}, FF of 86.28%, and PCE of 27.20%.

AZO UTL/ZnO layer interface defect density is varied from 1×10^5 cm^{-2} to 1×10^{15} cm^{-2}. As depicted in Fig. 14(c), V_{oc} remains fixed at 1.3221 V as N_{it} increases from 1×10^5 cm^{-2} to 1×10^{15} cm^{-2}. J_{sc} remains constant at 23.84 mA cm^{-2} as N_{it} enhances between 1×10^5 cm^{-2} and 1×10^{13} cm^{-2}, subsequently slightly decreases to 2383 mA cm^{-2} at 1×10^{14} cm^{-2}, and then slightly decreases to 23.82 mA cm^{-2} at 1×10^{14} cm^{-2}. FF remains constant at 86.28% when N_{it} increases from 1×10^5 cm^{-2} to 1×10^{15} cm^{-2}. PCE has a fixed value of 27.20% as N_{it} increases from 1×10^5 cm^{-2} to 1×10^{13} cm^{-2}; at that point, it decreases to 27.19% at 1×10^{14} cm^{-2}; and 27.18% at 1×10^{15} cm^{-2}. The optimum value of this interface defect density occurs at 1×10^{13} cm^{-2}, and the PV output parameters are as follows: V_{oc} of 1.3221 V, J_{sc} of 23.84 mA cm^{-2}, FF of 86.28%, and PCE of 27.20%.

In this article, we achieved an efficiency of 27.18% by optimizing the thickness, defect density, and acceptor doping concentration of the Cs_2BiAgI_6 absorber layer. Here, we want to find the optimum value of the defect density for ETL and HTL. Fig. 9 shows that the optimal defect density for the V_2O_5-HTL is 1×10^{17} cm^{-3} (PCE = 27.18%). In Fig. 11, the optimal defect density for the AZO UTL-ETL is 1×10^{16} cm^{-3} (PCE = 27.19%), while Fig. 13 depicts that the ZnO-ETL layer's optimal defect density is also $1 \times$ cm^{-3} (PCE = 27.20%). Finally, Fig. 14(c) illustrates the optimal interface defect density for AZO/ZnO as 1×10^{13} cm^{-2} (PCE = 27.20%).[89] The *J–V–T* (current density *vs.* voltage for various temperatures) and *C–f–T* (capacitance vs frequency for various temperatures) measurements can help researchers to determine the defect properties in the perovskite solar cell. Using the *J–V–T* technique, the *J–V* curves can be measured at different temperatures. After obtaining the amount of V_{oc}, and plotting it against different temperatures, this linear curve intersection with the V_{oc}-axis gives E_t/q (E_t: defect energy, q: electron charge); the amount of E_t is required in the SCAPS program.[90] We can also calculate the *C–f* curves for different temperatures and *C–f–T* (thermal admittance analysis, TAS method) using the SCAPS package, which might allow us to calculate the defect density as a function of defect energy $N_t(E_t)$ from a set of $C(f, T)$ experimental measurements. More information regarding the parameters (such as V_{bi}, built-in voltage) could be obtained by referring to the Mott–Schottky analysis, specifically ($1/C^2$ *vs.* V).[91,92] Moreover, some other techniques are available for considering the defect properties, such as temperature-dependent space charge limited current (SCLC); deep-level transient spectroscopy (DLTS); Laplace current DLTS (I-DLTS); steady-state photoluminescence (SSPL); time-resolved photoluminescence (TRPL); PL mapping; time-resolved microwave conductivity (TRMC); thermally stimulated current (TSC); transient photocapacitance (TPC); surface photovoltage (SPV) spectroscopy; and time-resolved spectroscopies such as transient absorption and reflection techniques, ultraviolet photoemission spectroscopy (UPS), and scanning tunneling microscopy (STM).[93]

3.12. Influence of the work function of back metal contact on Cs_2BiAgI_6-DPSC performance

For the enhanced PCE of Cs_2BiAgI_6-DPSC, the back metal contact's work function is a critical factor. The value of ϕ_{BC} (work function) directly impacts the presence of an appropriate built-in electric field in Cs_2BiAgI_6-DPSC,[94] affecting the electric field that aids in hole transport and collection; thus, ϕ_{BC} significantly influences V_{oc}.[95] To study the effect of different back electrode ϕ_{BC} values on Cs_2BiAgI_6-DPSC performance, we explored ϕ_{BC} ranging from 4.65 eV to 5.9 eV.[96] Our findings from simulations are presented in Fig. 15.

The work function of the back metal contact is a critical parameter for increasing the PCE of the Cs_2BiAgI_6-DPSC. The value of ϕ_{BC} directly affects the presence of an appropriate built-in electric field in the Cs_2BiAgI_6-DPSC, which in turn influences the transport and collection of holes and ultimately determines the V_{oc}. To investigate the impact of different ϕ_{BC} values on the performance of the Cs_2BiAgI_6-DPSC, we conducted simulations with ϕ_{BC} ranging from 4.65 eV to 5.9 eV. The work functions of different materials for back electrodes are as follows: Cu (4.65 eV), Fe (4.81 eV), C (5 eV), Au (5.1 eV), W (5.22 eV), Ni (5.5 eV), Pd (5.6 eV), Pt (5.7 eV), and Se (5.9 eV).[96] Fig. 15(a) illustrates that at low ϕ_{BC} values, the *J–V* curves display an S-shaped pattern because of the presence of elevated Schottky barriers at the interface between the HTL and back metal contact, leading to an impediment in hole transfer and a decrease in the FF.[97,98] Copper (4.65 eV) and iron (4.81 eV) showed this phenomenon in our study. Fig. 15(b) presents the PV parameters of the device ITO/ZnO/AZO/Cs_2BiAgI_6 (650 nm)/V_2O_5/BC for different ϕ_{BC} values ranging from 4.65 eV to 5.9 eV. The highest efficiency of 27.20% was reached with Ni, Pd, Pt, or Se as the back metal contact, as depicted in Fig. 15(b).

As the work function of the back electrode decreases, the Schottky barrier gradually increases, leading to a higher energy requirement for holes to pass through the barrier. This hinders the transport of holes to the back metal contact,[94] which ultimately impedes the effective collection of holes and causes a gentle decrease in V_{oc}, thereby reducing efficiency. By utilizing a back electrode with a high work function, the Fermi level

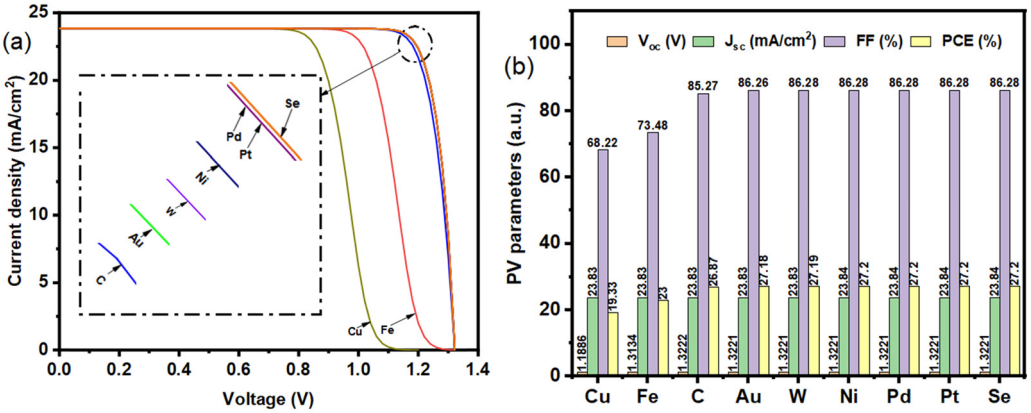

Fig. 15 (a) *J–V* curve. Inset of the figure shows C (Carbon), Au (Gold), W (Tungsten), Ni (Nickel), Pd (Palladium), Pt (Platinum), and Se (Selenium) work functions. (b) PV parameters as a bar chart against different work functions of Cs_2BiAgI_6-DPSCs ranging from 4.65 eV to 5.9 eV.

is lowered, facilitating the formation of improved Ohmic contacts.[99] Therefore, selecting the appropriate back contact material is crucial for achieving high efficiency in Cs_2BiAgI_6-DPSCs. It is essential to ensure that the V_2O_5-HTL and back contact form an ohmic contact at the interface to prevent the formation of a high Schottky barrier. Incorporating a low-cost metal, such as Se, as the back contact, as shown in Fig. 15(b), can significantly enhance the efficiency of Cs_2BiAgI_6-DPSCs.

3.13. Influence of working temperature on Cs_2BiAgI_6-DPSC performance

When Cs_2BiAgI_6-DPSCs are exposed to high temperatures, the performance parameters are affected by the temperature.[100] An increase in temperature results in a decrease in V_{oc} and a slight increase in J_{sc} of Cs_2BiAgI_6-DPSC.[101–103]

Cs_2BiAgI_6-DPSCs are typically used in outdoor settings where temperatures exceed 300 K,[104] the outdoor temperature directly affects the performance of Cs_2BiAgI_6-DPSCs. Investigating temperature's impact on Cs_2BiAgI_6-DPSC, T ranges from 300 K to 500 K. As temperature increases, V_{oc} decreases, lowering Cs_2BiAgI_6-DPSC PCE.[105] As temperature increases, the defect density in the device increases, and mobility decreases, hurting Cs_2BiAgI_6-DPSC performance.[106] Changes in temperature greatly affect the performance of Cs_2BiAgI_6-DPSC through its impact on V_{oc}. The relationship between V_{oc} and T can be expressed as follows:[105]

$$\frac{dV_{oc}}{dT} = \frac{V_{oc} - \frac{E_g}{q}}{T}. \quad (16)$$

Eqn (16) reveals an inverse relationship between V_{oc} and T. An increase in T leads to a decrease in V_{oc} and an increase in the diode reverse saturation current.[104]

The results from Fig. 16 indicate that the performance of the Cs_2BiAgI_6-DPSCs significantly decreases as the operating temperature increases. This is because R_S increases with temperature, which reduces diffusion length and increases recombination rate. Consequently, the FF and efficiency of the Cs_2BiAgI_6-DPSC decreases.[106,107]

In Fig. 16a–d, the PV output parameters are plotted against various temperatures, which vary from 300 K to 500 K in 11 steps. According to Fig. 16(a), V_{oc} diminishes from 1.3221 V to 1.0501 V. In Fig. 16(b), J_{sc} increases from 23.84011 mA cm^{-2} at 300 K to 23.85634 mA cm^{-2} at 500 K. As depicted in Fig. 16(c), FF decreases from 86.28% to 76.25%. In Fig. 16(d), PCE decreases from 27.20% to 19.10%. At 300 K, the optimum value is obtained, with the following PV output parameters: V_{oc} of 1.3221 V, J_{sc} of 23.84 mA cm^{-2}, FF of 86.28%, and PCE of 27.20%.

3.14. Comparing the results of ITO/ZnO/AZO/Cs_2BiAgI_6 (650 nm)/V_2O_5/Se device before and after optimization

Fig. 17 presents the results of before and after optimization for (a) the *J–V* curve (Table S7 and Fig. S5, ESI†) and (b) the EQE curve of ITO/ZnO/AZO/Cs_2BiAgI_6 (650 nm)/V_2O_5/Se device. Regarding the EQE curve, prior to optimization, it initiates at 27.806% (300 nm), increases to 99.765% (360 nm), and then remains relatively constant until 550 nm (99.416%) before decreasing to zero at 780 nm. Following optimization, the EQE curve commences at 27.789% (300 nm), increases to 99.849% (355 nm), reaches its peak at 100% (377 nm), maintains a nearly constant value until 550 nm (99.662%), and eventually decreases to zero at 780 nm, as illustrated in Fig. 17(b). Table 6 illustrates the comparison of the results of the *J–V* curve before and after optimization for ITO/ZnO/AZO/Cs_2BiAgI_6 (650 nm)/V_2O_5/Se device.

3.15. Comparing our investigation results with those of previous studies

The electron transport layer plays a vital role in facilitating the movement of charge carriers within DPSCs to achieve the Shockley–Queisser limit. Employing a bilayer electron transport layer (ZnO/AZO) demonstrates superior charge transfer capabilities and enhanced charge collection, leading to a decrease in trap-assisted recombination at the interface. Comprehensive findings suggest that the utilization of a bilayer electron transport layer presents an efficient approach to improving the interface and fabricating high-performing planar double

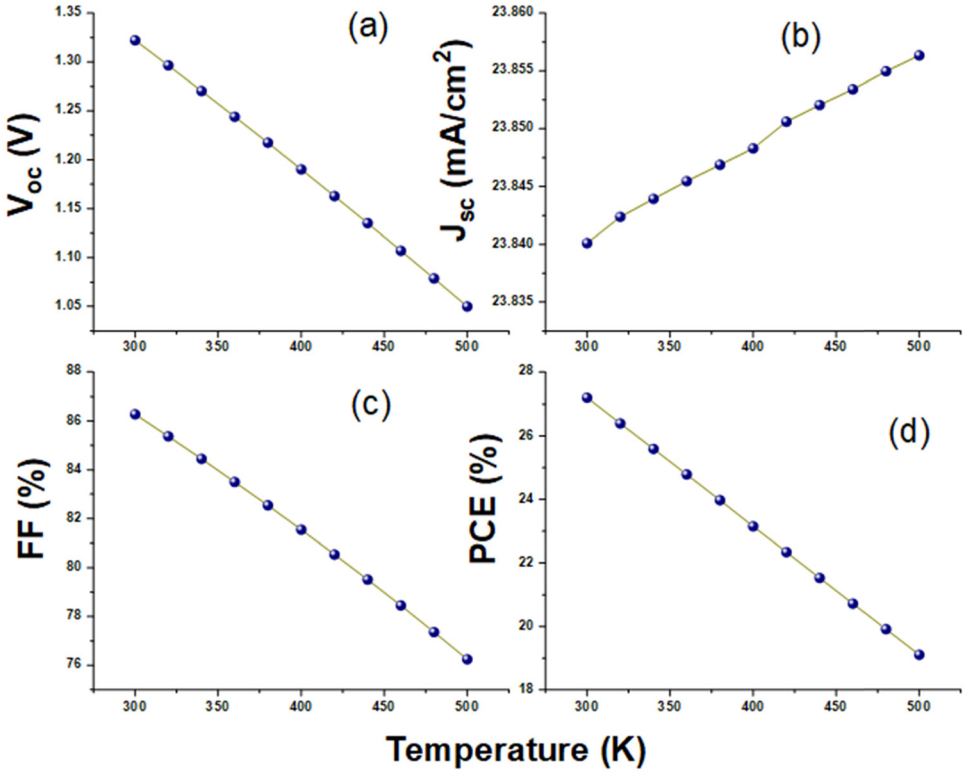

Fig. 16 PV output parameters: (a) V_{oc}, (b) J_{sc}, (c) FF, and (d) PCE for Cs_2BiAgI_6-DPSC against temperature.

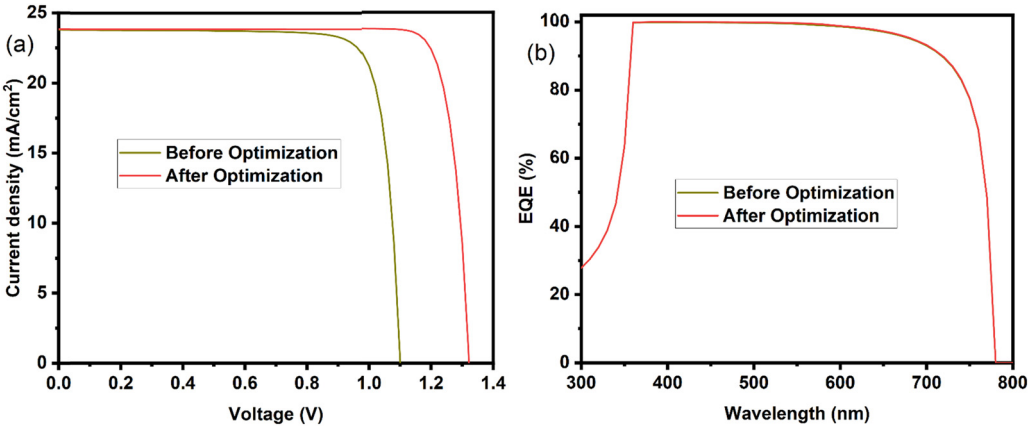

Fig. 17 Comparing the results of before and after optimization for ITO/ZnO/AZO/Cs_2BiAgI_6 (650 nm)/V_2O_5/Se device: (a) *J*–*V* curve and (b) EQE curve.

perovskite solar cells. Table 7 provides a comparison of the PV output parameters for different double perovskite solar cells and our results.

Table 6 Comparing the results of the *J*–*V* curve before and after optimization for ITO/ZnO/AZO/Cs_2BiAgI_6 (650 nm)/V2O5/Se device

Parameter	V_{oc} (V)	J_{sc} (mA cm^{-2})	FF (%)	PCE (%)
Before optimization	1.1005	23.78	82.78	21.67
After optimization	1.3221	23.84	86.28	27.20

4. Conclusion

Toxic metals in perovskite solar cells hinder their commercialization. Double halide perovskites have garnered significant interest owing to their reduced toxicity, adaptable bandgap, structural versatility, and enhanced stability when compared to conventional lead halide perovskites. This study focused on assessing the performance of lead-free Cs_2BiAgI_6-double perovskite solar cells (DPSCs) using a one-dimensional solar cell capacitance simulator (SCAPS-1D) with bilayer ZnO/AZO ETL and ZnO ETL, in addition to various HTLs for the first time. The

Table 7 Comparison of PV output parameters for different double perovskite solar cells

Device configuration	V_{oc} (V)	J_{sc} (mA cm^{-2})	FF	PCE (%)	Procedure	Ref.
FTO/c-TiO_2/m-TiO_2/$Cs_2AgBiBr_6$/Spiro-OMeTAD/Au	0.98	3.93	0.63	2.43	Experiment	108
ITO/c-TiO_2/$Cs_2AgBiBr_6$/Spiro-OMeTAD/Au	1.06	1.55	0.74	1.22	Experiment	109
ITO/SnO_2/$Cs_2AgBiBr_6$/P_3HT/Au	1.04	1.78	0.78	1.44	Experiment	110
FTO/c-TiO_2/$Cs_2AgBiBr_6$/P_3HT/Au	1.12	1.79	0.68	1.37	Experiment	111
ITO/c-TiO_2/$Cs_2AgBiBr_6$/Spiro-OMeTAD/MoO_3/Au	1.05	2.06	0.65	1.41	Experiment	112
ITO/Cu–NiO/$Cs_2AgBiBr_6$/C60/BCP/Ag	1.01	3.19	0.69	2.23	Experiment	113
FTO/c-TiO_2/C–Chl m-TiO_2/$Cs_2AgBiBr_6$/Spiro-OMeTAD/Ag	1.04	4.09	0.73	3.11	Experiment	114
FTO/c-TiO_2/m-TiO_2/D149/$Cs_2AgBiBr_6$-$Ti_3C_2T_x$/Spiro-OMeTAD/Ag	0.722	8.85	0.701	4.47	Experiment	115
ITO/SnO_2/$Cs_2AgBiBr_6$/Zn–Chl/Ag	0.99	3.83	0.736	2.79	Experiment	116
FTO/c-TiO_2/m-TiO_2/$Cs_2AgSb_{0.25}Bi_{0.75}Br_6$/Spiro-OMeTAD/Au	0.64	1.03	0.38	0.25	Experiment	117
ITO/ZnO/AZO/Cs_2BiAgI_6 (650 nm)/V_2O_5/Se	1.322	23.84	0.863	27.20	This work	

HTLs selected for evaluation included CBTS, Cu_2O, $CuAlO_2$, CZTS, CuSCN, spiro-OMeTAD, MoO_3, and V_2O_5. Several parameters, such as energy band alignment, recombination and generation rates, absorber thickness, defect and doping densities for all layers, energy levels of ETLs and HTL, interfacial defect densities, back metal contact, and operating temperature, were investigated to enhance the efficiency of the DPSC. Simulation works on the most effective cells were carried out to gain a comprehensive understanding of the electrical characteristics of the device, which demonstrated that these interfacial bilayers significantly enhanced the photovoltaic properties and overall performance of the device. This research also aimed to boost the efficiency and deepen our comprehension of electron transport mechanisms in Cs_2BiAgI_6-DPSCs. Results indicated that V_2O_5 and ZnO/AZO were the most appropriate materials for HTL and ETL, respectively, among the various options considered. Consequently, the required DPSC was opted as ITO/ZnO/AZO/Cs_2BiAgI_6/V_2O_5/Au. To achieve high performance in planar DPSCs, optimizing the extraction and recombination of electron–hole pairs at the ETL/perovskite interface is crucial. The main concept involved enhancing the ZnO/double perovskite interface properties by introducing a 10 nm ultra-thin layer (UTL) of AZO, which served as a passivation layer. The ZnO/AZO bilayer structure offered benefits, such as effective electron extraction and reduced interfacial recombination owing to its improved energy level alignment and defect passivation. The Cs_2BiAgI_6 absorber layer had a thickness of 650 nm, with a defect density of 1×10^{13} cm^{-3} and an acceptor density of 1×10^{16} cm^{-3}. The V_2O_5 layer had a defect density of 1×10^{17} cm^{-3} and its VBO_1 was 0.0 eV. The AZO layer had a defect density of 1×10^{16} cm^{-3} and its CBO_2 was 0.0 eV. The defect density of ZnO ($N_{t,ZnO}$) was 1×10^{16} cm^{-3}. The interface defect density achieved for the V_2O_5/Cs_2BiAgI_6 side was 1×10^{10} cm^{-2} and for the Cs_2BiAgI_6/AZO side, it was 1×10^{10} cm^{-2}. For the AZO/ZnO side interface, the defect density was 1×10^{13} cm^{-2}. Selenium (Se) was chosen as the back metal contact and the temperature was set at 300 K. Upon fine-tuning these factors, the efficiency of the ZnO/AZO bilayer ETL system reached 27.20%, together with a V_{oc} of 1.3221 V, J_{sc} of 23.84 mA cm^{-2} and an FF of 86.28%. Thus, this study introduces a direct and promising method for producing photovoltaic devices, especially for various double perovskite types, featuring advantageous charge transport layers and recombination characteristics. Furthermore, these results offer a theoretical framework for enhancing the efficiency of Cs_2BiAgI_6-based photovoltaic solar cells (DPSCs), promoting the widespread use of environmentally friendly and durable perovskites.

Author contributions

Aminreza Mohandes: conceptualization, formal analysis, project administration, methodology, software, validation, data curation, writing original draft. Mahmood Moradi: supervision, conceptualization, writing, review and editing.

Data availability

All data that support the findings of this research are included in the article and its ESI.†

Conflicts of interest

The authors declare that they have no known competing financial interests or personal relationships that could have appeared to influence the work reported in this paper.

Acknowledgements

This research did not receive any specific grant from funding agencies in the public, commercial or not-for-profit sectors. The authors express their gratitude to Professor Marc Burgeleman from the Gent University, Belgium for developing the SCAPS-1D program and permitting its use.

References

1 A. Kojima, K. Teshima, Y. Shirai and T. Miyasaka, *J. Am. Chem. Soc.*, 2009, **131**, 6050–6051.
2 Y. Chen, L. Zhang, Y. Zhang, H. Gao and H. Yan, *RSC Adv.*, 2018, **8**, 10489–10508.
3 C. O. R. Quiroz, Y. Shen, M. Salvador, K. Forberich, N. Schrenker, G. D. Spyropoulos, T. Heumüller, B. Wilkinson, T. Kirchartz and E. Spiecker, *J. Mater. Chem. A*, 2018, **6**, 3583–3592.

4 K. Yoshikawa, H. Kawasaki, W. Yoshida, T. Irie, K. Konishi, K. Nakano, T. Uto, D. Adachi, M. Kanematsu, H. Uzu and K. Yamamoto, *Nat. Energy*, 2017, **2**, 17032.
5 N. Kumar, J. Rani and R. Kurchania, *Sol. Energy*, 2021, **221**, 197–205.
6 M. Samiul Islam, K. Sobayel, A. Al-Kahtani, M. A. Islam, G. Muhammad, N. Amin, M. Shahiduzzaman and M. Akhtaruzzaman, *Nanomaterials*, 2021, **11**, 1218.
7 S. M. Majeed, D. S. Ahmed and M. K. A. Mohammed, *Org. Electron.*, 2021, **99**, 106310.
8 M. K. A. Mohammed, S. Singh, A. K. Al-Mousoi, R. Pandey, J. Madan, D. Dastan and G. Ravi, *RSC Adv.*, 2022, **12**, 32611–32618.
9 Q. Wang, X. Zhang, Z. Jin, J. Zhang, Z. Gao, Y. Li and S. F. Liu, *ACS Energy Lett.*, 2017, **2**, 1479–1486.
10 J. Jiang, Z. Jin, J. Lei, Q. Wang, X. Zhang, J. Zhang, F. Gao and S. F. Liu, *J. Mater. Chem. A*, 2017, **5**, 9514–9522.
11 A. Mathur and V. Maheshwari, *J. Mater. Chem. C*, 2022, **10**, 7485–7493.
12 Y. Raoui, H. Ez-Zahraouy, S. Ahmad and S. Kazim, *Sustainable Energy Fuels*, 2021, **5**, 219–229.
13 A. Babayigit, A. Ethirajan, M. Muller and B. Conings, *Nat. Mater.*, 2016, **15**, 247–251.
14 I. R. Benmessaoud, A. L. Mahul-Mellier, E. Horváth, B. Maco, M. Spina, H. A. Lashuel and L. Forró, *Toxicol. Res.*, 2016, **5**, 407–419.
15 A. Babayigit, D. Duy Thanh, A. Ethirajan, J. Manca, M. Muller, H.-G. Boyen and B. Conings, *Sci. Rep.*, 2016, **6**, 18721.
16 O. A. Lozhkina, A. A. Murashkina, M. S. Elizarov, V. V. Shilovskikh, A. A. Zolotarev, Y. V. Kapitonov, R. Kevorkyants, A. V. Emeline and T. Miyasaka, *Chem. Phys. Lett.*, 2018, **694**, 18–22.
17 R. E. Brandt, R. C. Kurchin, R. L. Z. Hoye, J. R. Poindexter, M. W. B. Wilson, S. Sulekar, F. Lenahan, P. X. T. Yen, V. Stevanovic and J. C. Nino, *J. Phys. Chem. Lett.*, 2015, **6**, 4297–4302.
18 H. Zhou, Q. Chen, G. Li, S. Luo, T. Song, H.-S. Duan, Z. Hong, J. You, Y. Liu and Y. Yang, *Science*, 2014, **345**, 542–546.
19 F. Giustino and H. J. Snaith, *ACS Energy Lett.*, 2016, **1**, 1233–1240.
20 F. Jiang, D. Yang, Y. Jiang, T. Liu, X. Zhao, Y. Ming, B. Luo, F. Qin, J. Fan and H. Han, *J. Am. Chem. Soc.*, 2018, **140**, 1019–1027.
21 E. T. McClure, M. R. Ball, W. Windl and P. M. Woodward, *Chem. Mater.*, 2016, **28**, 1348–1354.
22 P.-K. Kung, M.-H. Li, P.-Y. Lin, J.-Y. Jhang, M. Pantaler, D. C. Lupascu, G. Grancini and P. Chen, *Sol. RRL*, 2020, **4**, 1900306.
23 K. Dave, M. H. Fang, Z. Bao, H. T. Fu and R. S. Liu, *Chem. – Asian J.*, 2020, **15**, 242–252.
24 C. Frangville, M. Rutkevičius, A. P. Richter, O. D. Velev, S. D. Stoyanov and V. N. Paunov, *ChemPhysChem*, 2012, **13**, 4235–4243.
25 P. K. Nayak, D. T. Moore, B. Wenger, S. Nayak, A. A. Haghighirad, A. Fineberg, N. K. Noel, O. G. Reid, G. Rumbles and P. Kukura, *Nat. Commun.*, 2016, **7**, 13303.
26 F. Marchetti, E. Moroni, A. Pandini and G. Colombo, *J. Phys. Chem. Lett.*, 2021, **12**, 3724–3732.
27 A. H. Slavney, T. Hu, A. M. Lindenberg and H. I. Karunadasa, *J. Am. Chem. Soc.*, 2016, **138**, 2138–2141.
28 G. Volonakis, M. R. Filip, A. A. Haghighirad, N. Sakai, B. Wenger, H. J. Snaith and F. Giustino, *J. Phys. Chem. Lett.*, 2016, **7**, 1254–1259.
29 F. Igbari, Z. Wang and L. Liao, *Adv. Energy Mater.*, 2019, **9**, 1803150.
30 X.-G. Zhao, D. Yang, J.-C. Ren, Y. Sun, Z. Xiao and L. Zhang, *Joule*, 2018, **2**, 1662–1673.
31 H. Absike, N. Baaalla, R. Lamouri, H. Labrim and H. Ez-zahraouy, *Int. J. Energy Res.*, 2022, **46**, 11053–11064.
32 H. Wu, A. Erbing, M. B. Johansson, J. Wang, C. Kamal, M. Odelius and E. M. J. Johansson, *ChemSusChem*, 2021, **14**, 4507–4515.
33 M. I. Kholil, M. T. H. Bhuiyan, M. A. Rahman, M. S. Ali and M. Aftabuzzaman, *RSC Adv.*, 2021, **11**, 2405–2414.
34 M. Roknuzzaman, K. Ostrikov, H. Wang, A. Du and T. Tesfamichael, *Sci. Rep.*, 2017, **7**, 14025.
35 J. U. Rehman, M. Usman, S. Amjid, M. Sagir, M. B. Tahir, A. Hussain, I. Alam, R. Nazir, H. Alrobei and S. Ullah, *Comput. Theor. Chem.*, 2022, **1209**, 113624.
36 M. A. Hadi, M. N. Islam and J. Podder, *RSC Adv.*, 2022, **12**, 15461–15469.
37 A. Mohandes and M. Moradi, *Phys. Scr.*, 2024, **99**, 55951.
38 J. Dong, Y. Zhao, J. Shi, H. Wei, J. Xiao, X. Xu, J. Luo, J. Xu, D. Li and Y. Luo, *Chem. Commun.*, 2014, **50**, 13381–13384.
39 Z.-L. Tseng, C.-H. Chiang, S.-H. Chang and C.-G. Wu, *Nano Energy*, 2016, **28**, 311–318.
40 S.-H. Wu, M.-Y. Lin, S.-H. Chang, W.-C. Tu, C.-W. Chu and Y.-C. Chang, *J. Phys. Chem. C*, 2018, **122**, 236–244.
41 C. Bhoomanee, P. Ruankhama, S. Choopun, A. Prathan and D. Wongratanaphisan, *Mater. Today Proc.*, 2019, **17**, 1259–1267.
42 F. Khan and J. H. Kim, *Solid State Electrochem.*, 2020, **164**, 107714.
43 A. Guchhait, G. K. Dalapati, P. Sonar, S. Gopalan, F. Bin Suhaimi, T. Das, V. G. V. Dutt, N. Mishra, C. Mahata and A. Kumar, *J. Electron. Mater.*, 2021, **50**, 5732–5739.
44 J. Kruszyńska, J. Ostapko, V. Ozkaya, B. Surucu, O. Szawcow, K. Nikiforow, M. Hołdyński, M. M. Tavakoli, P. Yadav and M. Kot, *Adv. Mater. Interfaces*, 2022, **9**, 2200575.
45 S. A. Moiz, A. N. M. Alahmadi and A. J. Aljohani, *IEEE Access*, 2021, **9**, 54254–54263.
46 M. Burgelman, P. Nollet and S. Degrave, *Thin Solid Films*, 2000, **361–362**, 527–532.
47 M. K. Hossain, A. A. Arnab, R. C. Das, K. M. Hossain, M. H. K. Rubel, M. F. Rahman, H. Bencherif, M. E. Emetere, M. K. A. Mohammed and R. Pandey, *RSC Adv.*, 2022, **12**, 35002–35025.
48 A. Mohandes, M. Moradi and M. Kanani, *Opt. Quantum Electron.*, 2023, **55**, 533.
49 J. C. Z. Medina, E. R. Andrés, C. M. Ruíz, E. C. Espinosa, L. T. Yarce, R. G. Isasmendi, R. R. Trujillo, G. G. Salgado,

A. C. Solis and F. G. N. Caballero, *Heliyon*, 2023, **9**(3), e14547.
50 K. T. Arockiya Dass, M. K. Hossain and L. Marasamy, *Sci. Rep.*, 2024, **14**, 1473.
51 L. R. Karna, R. Upadhyay and A. Ghosh, *Sci. Rep.*, 2023, **13**, 15212.
52 A. Mohandes, M. Moradi and H. Nadgaran, *Opt. Quantum Electron.*, 2021, **53**, 1–22.
53 M. Noman, I. N. Khan, A. Qamar, K. AlSnaie and H. M. H. Farh, *ACS Omega*, 2024, **9**(10), 11398–11417.
54 A. Mohandes, M. Moradi and H. Nadgaran, *Eur. Phys. J. Plus*, 2021, **136**, 113.
55 P. Rafieipour, A. Mohandes, M. Moaddeli and M. Kanani, Integrating transfer matrix method into SCAPS-1D for addressing optical losses and per-layer optical properties in perovskite/Silicon tandem solar cells, *arXiv*, 2023, preprint, arXiv:2308.01132, DOI: 10.48550/arXiv.2308.01132.
56 S. Bhattarai, M. K. Hossain, G. F. I. Toki, R. Pandey, J. Madan, D. P. Samajdar, S. Ezzine, L. Ben Farhat, M. Z. Ansari and S. H. Ahammad, *New J. Chem.*, 2023, **47**, 17908–17922.
57 A. Kuddus, M. F. Rahman, S. Ahmmed, J. Hossain and A. B. M. Ismail, *Superlattices Microstruct.*, 2019, **132**, 106168.
58 Q. Guo, C. Wang, J. Li, Y. Bai, F. Wang, L. Liu, B. Zhang, T. Hayat, A. Alsaedi and Z. Tan, *Phys. Chem. Chem. Phys.*, 2018, **20**, 21746–21754.
59 X. Yao, J. Qi, W. Xu, X. Jiang, X. Gong and Y. Cao, *ACS Omega*, 2018, **3**, 1117–1125.
60 Z. Liu, T. He, H. Wang, X. Song, H. Liu, J. Yang, K. Liu and H. Ma, *RSC Adv.*, 2017, **7**, 18456–18465.
61 H. Park, S. Jeong, E. Kim, S. Shin and H. Shin, *ACS Appl. Mater. Interfaces*, 2022, **14**, 42007–42017.
62 M. F. Hossain, A. Ghosh, M. A. Al Mamun, A. A. Miazee, H. Al-lohedan, R. J. Ramalingam, M. F. I. Buian, S. R. I. Karim, M. Y. Ali and M. Sundararajan, *Opt. Commun.*, 2024, **559**, 130410.
63 J. Li, J. Qin, X. Liu, M. Ren, J. Tong, N. Zheng, W. Chen and Y. Xia, *Sol. Energy*, 2020, **211**, 1102–1109.
64 J. Tian, Q. Xue, Q. Yao, N. Li, C. J. Brabec and H. Yip, *Adv. Energy Mater.*, 2020, **10**, 2000183.
65 J. Zhang, G. Hodes, Z. Jin and S. Liu, *Angew. Chem., Int. Ed.*, 2019, **58**, 15596–15618.
66 Q. Tai, K.-C. Tang and F. Yan, *Energy Environ. Sci.*, 2019, **12**, 2375–2405.
67 W. L. Lachore, D. M. Andoshe, M. A. Mekonnen, N. A. Tegegne and F. G. Hone, Highly crystalline metal oxide semiconductor electron transport bilayers to improve the interface between the electron transport and active layer in planar perovskite solar cells, *Research Square*, 2022, pp. 1–24, DOI: 10.21203/rs.3.rs-2136665/v1.
68 P. Schulz, L. L. Whittaker-Brooks, B. A. MacLeod, D. C. Olson, Y.-L. Loo and A. Kahn, *Adv. Mater. Interfaces*, 2015, **2**(7), 1400532.
69 M. H. K. Rubel, M. A. Hossain, M. K. Hossain, K. M. Hossain, A. A. Khatun, M. M. Rahaman, M. F. Rahman, M. M. Hossain and J. Hossain, *Results Phys.*, 2022, **42**, 105977.
70 M. Rai, L. H. Wong and L. Etgar, *J. Phys. Chem. Lett.*, 2020, **11**, 8189–8194.
71 T. Singh, A. Kulkarni, M. Ikegami and T. Miyasaka, *ACS Appl. Mater. Interfaces*, 2016, **8**, 14542–14547.
72 W. Chang, H. Tian, G. Fang, D. Guo, Z. Wang and K. Zhao, *Sol. Energy*, 2019, **186**, 323–327.
73 P. Zhao, Z. Liu, Z. Lin, D. Chen, J. Su, C. Zhang, J. Zhang, J. Chang and Y. Hao, *Sol. Energy*, 2018, **169**, 11–18.
74 J. Barbé, M. L. Tietze, M. Neophytou, B. Murali, E. Alarousu, A. El Labban, M. Abulikemu, W. Yue, O. F. Mohammed, I. McCulloch, A. Amassian and S. Del Gobbo, *ACS Appl. Mater. Interfaces*, 2017, **9**, 11828–11836.
75 H. Kim, K. G. Lim and T. W. Lee, *Energy Environ. Sci.*, 2016, **9**, 12–30.
76 D. Chen, Y. Wang, Z. Lin, J. Huang, X. Chen, D. Pan and F. Huang, *Cryst. Growth Des.*, 2010, **10**, 2057–2060.
77 Y. Chen, H. Shen and P. P. Altermatt, *Sol. Energy Mater. Sol. Cells*, 2014, **120**, 356–362.
78 Q. Wang, Y. Shao, H. Xie, L. Lyu, X. Liu, Y. Gao and J. Huang, *Appl. Phys. Lett.*, 2014, **105**, 163508.
79 M. Abdi-Jalebi, M. I. Dar, A. Sadhanala, S. P. Senanayak, M. Grätzel and R. H. Friend, *JoVE*, 2017, e55307.
80 M. S. Jamal, S. A. Shahahmadi, M. A. A. Wadi, P. Chelvanathan, N. Asim, H. Misran, M. I. Hossain, N. Amin, K. Sopian and M. Akhtaruzzaman, *Optik*, 2019, **182**, 1204–1210.
81 S. Bouazizi, W. Tlili, A. Bouich, B. M. Soucase and A. Omri, *Mater. Res. Express*, 2022, **9**, 96402.
82 K. S. Nithya and K. S. Sudheer, *Optik*, 2020, **217**, 164790.
83 T. Minemoto and M. Murata, *Sol. Energy Mater. Sol. Cells*, 2015, **133**, 8–14.
84 K. D. A. Kumar, S. Valanarasu, S. R. Rosario, V. Ganesh, M. Shkir, C. J. Sreelatha and S. AlFaify, *Solid State Sci.*, 2018, **78**, 58–68.
85 D. Thakur, S.-E. Chiang, M.-H. Yang, J.-S. Wang and S. H. Chang, *Sol. Energy Mater. Sol. Cells*, 2022, **235**, 111454.
86 D. K. Sarkar, A. K. M. Hasan, M. Mottakin, V. Selvanathan, K. Sobayel, M. A. Islam, G. Muhammad, M. Aminuzzaman, M. Shahiduzzaman and K. Sopian, *Sol. Energy*, 2022, **243**, 215–224.
87 G. Pindolia, S. M. Shinde and P. K. Jha, *Sol. Energy*, 2022, **236**, 802–821.
88 F. Izadi, A. Ghobadi, A. Gharaati, M. Minbashi and A. Hajjiah, *Optik*, 2021, **227**, 166061.
89 A. S. Chouhan, N. P. Jasti and S. Avasthi, *Mater. Lett.*, 2018, **221**, 150–153.
90 S. Zahedi-Azad, M. Maiberg and R. Scheer, *Prog. Photovoltaics Res. Appl.*, 2020, **28**, 1146–1157.
91 M. Burgelman, Mott-Schottky analysis from C-V simulations, and Admittance Analysis from C-f simulations in SCAPS, Dept. of Electronics and Information Technology (ELIS), University of Gent, Belgium, 2017, 2–4.
92 T. Walter, R. Herberholz, C. Müller and H. W. Schock, *J. Appl. Phys.*, 1996, **80**, 4411–4420.
93 L. K. Ono, S. Liu and Y. Qi, *Angew. Chem., Int. Ed.*, 2020, **59**, 6676–6698.
94 L. Lin, L. Jiang, P. Li, B. Fan and Y. Qiu, *J. Phys. Chem. Solids*, 2019, **124**, 205–211.

95 D. Qiu and E. K. Kim, *Sci. Rep.*, 2015, **5**, 13743.
96 K. D. Jayan and V. Sebastian, *Sol. Energy*, 2021, **217**, 40–48.
97 L. Lin, L. Jiang, Y. Qiu and B. Fan, *J. Phys. Chem. Solids*, 2018, **122**, 19–24.
98 J. Gao, J. M. Luther, O. E. Semonin, R. J. Ellingson, A. J. Nozik and M. C. Beard, *Nano Lett.*, 2011, **11**, 1002–1008.
99 J. Shewchun, J. Dubow, C. W. Wilmsen, R. Singh, D. Burk and J. F. Wager, *J. Appl. Phys.*, 1979, **50**, 2832–2839.
100 S. H. Liu, E. J. Simburger, J. Matsumoto, A. Garcia III, J. Ross and J. Nocerino, *Prog. Photovoltaics Res. Appl.*, 2005, **13**, 149–156.
101 M. Fathi, M. Abderrezek, F. Djahli and M. Ayad, *Energy Procedia*, 2015, **74**, 1410–1417.
102 H. Heriche, Z. Rouabah and N. Bouarissa, *Int. J. Hydrogen Energy*, 2017, **42**, 9524–9532.
103 M. Theelen, A. Liakopoulou, V. Hans, F. Daume, H. Steijvers, N. Barreau, Z. Vroon and M. Zeman, *J. Renewable Sustainable Energy*, 2017, **9**, 21205.
104 E. Karimi and S. M. B. Ghorashi, *J. Nanophotonics*, 2017, **11**, 32510.
105 N. Devi, K. A. Parrey, A. Aziz and S. Datta, *J. Vac. Sci. Technol., B: Nanotechnol. Microelectron.:Mater., Process., Meas., Phenom.*, 2018, **36**, 04G105.
106 F. Behrouznejad, S. Shahbazi, N. Taghavinia, H.-P. Wu and E. W.-G. Diau, *J. Mater. Chem. A*, 2016, **4**, 13488–13498.
107 S. R. Raga, E. M. Barea and F. Fabregat-Santiago, *J. Phys. Chem. Lett.*, 2012, **3**, 1629–1634.
108 E. Greul, M. L. Petrus, A. Binek, P. Docampo and T. Bein, *J. Mater. Chem. A*, 2017, **5**, 19972–19981.
109 W. Ning, F. Wang, B. Wu, J. Lu, Z. Yan, X. Liu, Y. Tao, J. Liu, W. Huang and M. Fahlman, *Adv. Mater.*, 2018, **30**, 1706246.
110 C. Wu, Q. Zhang, Y. Liu, W. Luo, X. Guo, Z. Huang, H. Ting, W. Sun, X. Zhong and S. Wei, *Adv. Sci.*, 2018, **5**, 1700759.
111 M. Wang, P. Zeng, S. Bai, J. Gu, F. Li, Z. Yang and M. Liu, *Sol. RRL*, 2018, **2**, 1800217.
112 F. Igbari, R. Wang, Z.-K. Wang, X.-J. Ma, Q. Wang, K.-L. Wang, Y. Zhang, L.-S. Liao and Y. Yang, *Nano Lett.*, 2019, **19**, 2066–2073.
113 W. Gao, C. Ran, J. Xi, B. Jiao, W. Zhang, M. Wu, X. Hou and Z. Wu, *ChemPhysChem*, 2018, **19**, 1696–1700.
114 B. Wang, N. Li, L. Yang, C. Dall'Agnese, A. K. Jena, S. Sasaki, T. Miyasaka, H. Tamiaki and X.-F. Wang, *J. Am. Chem. Soc.*, 2021, **143**, 2207–2211.
115 L. Yang, P. Hou, B. Wang, C. Dall'Agnese, Y. Dall'Agnese, G. Chen, Y. Gogotsi, X. Meng and X.-F. Wang, *Chem. Eng. J.*, 2022, **446**, 136963.
116 B. Wang, L. Yang, C. Dall'Agnese, A. K. Jena, S. Sasaki, T. Miyasaka, H. Tamiaki and X.-F. Wang, *Sol. RRL*, 2020, **4**, 2000166.
117 Y. Liu, L. Zhang, M. Wang, Y. Zhong, M. Huang, Y. Long and H. Zhu, *Mater. Today*, 2019, **28**, 25–30.